J. Fluid Mech. (1996), vol. 307, pp. 191–229

Stationary waves on an inclined sheet of viscous fluid at high Reynolds and moderate Weber numbers

By JENG-JONG LEE AND CHIANG C. MEI

Parsons Laboratory, Department of Civil and Environmental Engineering, Massachusetts Institute of Technology, Cambridge, MA 02139, USA

(Received 21 March 1995 and in revised form 25 September 1995)

A theory is described for the nonlinear waves on the surface of a thin film flowing down an inclined plane. Attention is focused on stationary waves of finite amplitude and long wavelength at high Reynolds numbers and moderate Weber numbers. Based on asymptotic equations accurate to the second order in the depth-to-wavelength ratio, a third-order dynamical system is obtained after changing to the frame of reference moving at the wave propagation speed. By examining the fixed-point stability of the dynamical system, parametric regimes of heteroclinc orbits and Hopf bifurcations are delineated. Extensive numerical experiments guided by the linear analyses reveal a variety of bifurcation scenarios as the phase speed deviates from the Hopf-bifurcation thresholds. These include homoclinic bifurcations which lead to homoclinic orbits corresponding to well separated solitary waves with one or several humps, some of which occur after passing through chaotic zones generated by period-doublings. There are also cases where chaos is the ultimate state following cascades of period-doublings, as well as cases where only limit cycles prevail. The dependence of bifurcation scenarios on the inclination angle, and Weber and Reynolds numbers is summarized.

1. Introduction

The flow of a thin layer of an incompressible viscous fluid down an inclined plane is a very old problem in fluid mechanics (Nusselt 1916). Much of the motivation for recent research stems from its practical applications in industrial processing. It is well known that finite-amplitude waves on film flows are relevant to devices such as adsorption columns, chemical reactors, steam condensors and vertical tube evaporators, since these waves enhance the transport of mass, heat and momentum across the liquid–gas and liquid–solid interfaces. In contrast, the formation of waves on the surface of a coating layer is highly undesirable in precision coating (Wang, Seaborg & Lin 1978). Therefore, following the pioneering work of Kapitza & Kapitza (1949), the literature on waves on a thin sheet of viscous layer is extensive. Since a comprehensive survey has been given recently by Chang (1994), we shall only mention a few papers to motivate the present study.

Many experiments on film waves have been reported in the literature. In some of them waves generated naturally were observed on a vertical plate (Tailby & Portalski 1962), or inside a vertical tube with a radius of a few centimetres (Stainthorp & Allen 1965; Jones & Whitaker 1966; Strobel & Whitaker 1969). Wavelength and wavespeeds of small-amplitude waves in the inception region were the most commonly measured

quantities. In most other experiments efforts were directed towards two-dimensional forced waves of finite amplitude (Kapitza & Kapitza 1949; Alekseenko, Nakoryakov & Pokusaev 1985). Kapitza & Kapitza (1949) generated regular two-dimensional waves by applying pulsations at the entrance of flow falling vertically along the outer surface of a circular cylinder. They reported that for a weak forcing at high frequencies, a train of near-sinusoidal periodic waves occurs downstream. On the other hand, a strong low-frequency forcing often generates a series of solitary waves possessing steep wavefronts and gently sloping tails, with ripples appearing ahead of the wavefronts.

Experiments have revealed that the properties of film waves change continuously as they propagate downstream, and may evolve into a highly irregular state far downstream (e.g. Kapitza & Kapitza 1949; Chu & Dukler 1974, 1975; Liu & Gollub 1993; Yu *et al.* 1995). Therefore a complete characterization of the wave field should include the spatial and temporal variations of wave amplitude, speed and length (or frequency) over a long distance and time, as well as their dependence on physical parameters such as the Reynolds and Weber numbers and the inclination angle. However, such comprehensive records are as yet unavailable. Most of the previous experiments were also conducted on the surface of cylinders of finite radius, rather than on a plane, and only over a limited fetch. Perhaps to bypass the difficulty of limited fetch, most investigators maintained artificial oscillations with a prescribed frequency which often is not the natural frequency of the most unstable mode. For example, Kapitza & Kapitza (1949) recorded the amplitude, speed, and wavelength of forced waves of a vertically falling water film in a tube for moderate Reynolds numbers ($5 < R < 20$) and large Weber numbers ($28 < W_e < 285$). The total length of the tube was too short (23 cm) for observing interesting bifurcations. Experiments by Stainthorp & Batt (1967) were similar. Only Takahama & Kato (1980) and Brauner & Maron (1982) described observations of film waves naturally formed on the surface film along a vertical cylinder and plate, respectively. Without artificial forcing, they showed that film waves always have irregular characters, and exhibit the phenomenon of apparent period-doubling (frequency reduction) and growing amplitude along the test section (2 and 1.6 m long, respectively). Evidence of chaos is particularly strong in the experiments of Chu & Dukler (1974, 1975) on the vertical water films flowing rapidly ($50 < R < 2000$, $0.01 < W_e < 7$) on the surface of a circular cylinder of 5 cm diameter. They analysed the statistical properties of the film thickness measured at 4.17 m below the top. Recently, Liu, Paul & Gollub (1993) and Liu & Gollub (1993, 1994) used high-precision optical techniques to study the flow development down a plane of 2 m length inclined at small angles ($4° \leqslant \theta \leqslant 10°$) for moderate Weber and Reynolds numbers ($3 < W_e < 33$; $6 < R < 26$). Aqueous solutions of glycerin were used. Similar to Kapitza & Kapitza (1949), they introduced artificial perturbations of varying amplitudes and frequencies at the entrance such that two-dimensional regular waves appeared slightly downstream. With measurement accuracy on the order of microns for the wave amplitude, they confirmed experimentally the theoretical critical condition (1.1) below, derived by Benjamin (1957) and Yih (1963) for the primary instability of the uniform flow. If f is the forcing frequency and R is the Reynolds number, the linear instability region in the f versus R plane is bounded above by the neutral curve f_n and below by the R-axis (see figures 3*a* and 17 later). Secondary instabilities of these forced waves were also found further downstream. Side-band instability occurs when the forcing frequency is relatively large, while period-doubling instability ensues when the forcing frequency is relatively small. At even larger Reynolds numbers, tertiary instabilities set in and spanwise variations of the free surface become significant (Liu, Schneider & Gollub 1995).

The theoretical literature can be divided into four categories: (i) linearized stability analyses; (ii) nonlinear theories for low or moderate Reynolds numbers; (iii) nonlinear theories for high Reynolds numbers; and (iv) direct numerical computations of the Navier–Stokes equations.

(i) *Linearized instability*: Yih (1955) was the first to formulate the eigenvalue problem based on the Orr–Sommerfeld equation. Benjamin (1957) subsequently incorporated surface tension. They found that the threshold for infinitesmal sine waves to be unstable is

$$\cot\theta/R < 6/5 \tag{1.1}$$

where θ is the inclination angle from the horizontal, and R is the Reynolds number defined by the unperturbed depth (H_0) and the depth-averaged velocity (u_0) of the uniform flow. For sufficiently thin film or long wavelength (L), i.e. $\epsilon = H_0/L \ll 1$ and $R \leqslant O(1)$, Yih (1963) gave approximate solutions valid up to $O(\epsilon^2 R^2)$. Additional numerical studies of the Orr–Sommerfeld equation have been carried out by many (Whitaker 1964; Anshus & Goren 1966; Krantz & Goren 1971; Pierson & Whitaker 1977) over a wider range of ϵ. See Lin (1983) for a more thorough review.

(ii) *Nonlinear theories for small R*: Subsequent efforts were focused on the nonlinear long waves in flows with relatively low Reynolds numbers: $R = O(1)$. Mei (1966) and Benney (1966) derived an evolution equation governing the flow depth, H, by a perturbation expansion technique in terms of the long-wave parameter ϵ. Omitting surface tension, Mei found monoclinal and polyclinal permanent waves, along with their amplitude-dispersion relations. Benney further deduced a Landau–Stuart equation describing the amplitude evolution of weakly nonlinear waves. Without surface tension, the second Landau coefficient turns out to be negative and hence nonlinear permanent waves of small-amplitude cannot exist. Three-dimensional extensions of this long-wave equation have been derived by Roskes (1970). Studies of the long-wave evolution equations with a strong surface tension, $W_e = O(\epsilon^{-2})$ where W_e is the Weber number defined later in (2.11), constitute the prevailing theme in the literature for low Reynolds number flows (Pumir, Manneville & Pomeau 1983; Nakaya 1989; Joo, Davis & Bankoff 1991). Other authors have studied the case of weak nonlinearity for which theories have been developed on three different bases: (*a*) an amplitude equation of Landau–Stuart type valid in the neighbourhood of the neutral curve in the ϵ versus R plane (Lin 1969, 1974; Gjevik 1970, 1971; Nakaya 1975); (*b*) modern bifurcation theory applied to weakly nonlinear permanent waves (Chang 1986, 1987, 1989); and (*c*) numerical solutions of the weakly nonlinear version of the long-wave evolution equation (the celebrated Kuramoto–Sivashingsky equation). The last approach has yielded a rich variety of solutions including limit cycles, homoclinic orbits, tori and chaotic attractors (Atherton 1972; Tougou 1981; Sivashinsky & Michelson 1980; Shlang & Sivashinsky 1982; Chen & Chang 1986; Hyman & Nicolaenko 1986; Tsvelodub & Trifonov 1989; Demekhin, Tokarev & Shkadov 1991; Trifonov 1992). See Chang (1994) for a review.

(iii) *Nonlinear theories for large R*: Relatively few papers have been devoted to nonlinear theories for high Reynolds numbers. Nearly all theories are for long waves, where the boundary layer and the momentum integral approximations have been applied for analytical convenience. The resulting nonlinear evolution equations are nevertheless still very complicated, and hence most studies concentrate on stationary (or permanent) waves whose speed and form do not change during the course of propagation. Furthermore, as in past studies for small to moderate R, surface tension is usually assumed to be large, $W_e = O(\epsilon^{-2})$, with the mathematical consequence that

the highest derivative appears at the leading order. In order to improve the boundary layer approximation, Sheintuch & Dukler (1989) extended the theory for flows down a vertical plate to second order $O(\epsilon^2)$. However, a uniform pressure distribution in the flow layer was assumed. As will be shown in §2, this approximation amounts to inconsistently omitting the $O(\epsilon^2)$ terms in the transverse momentum equation. They discovered a branch of limit cycles which, as the propagation speed is varied, undergo homoclinic bifurcations and eventually become homoclinic orbits. Similarly, Prokopiou, Cheng & Chang (1991) applied a second-order theory to flows on a nearly horizontal incline, and assumed a hydrostatic pressure distribution in the flow layer. With an assumed parabolic velocity profile and Kármán's momentum integral approximation, they used normal form theory to find analytical solutions such as limit cycles and homoclinic orbits near neutral stability. Some numerical solutions were obtained for fully nonlinear permanent waves, which include limit cycles followed by period-doubling bifurcations. Also for $R = O(\epsilon^{-1})$ and $W_e = O(\epsilon^{-2})$, Trifonov & Tsvelodub (1991) and Tsvelodub & Trifonov (1992) searched numerically for permanent waves of the leading-order system on a vertically falling flow and found only periodic and solitary waves. Recently, Chang, Demekhin & Kopelevich (1993) solved an approximate Navier–Stokes system valid up to $O(\epsilon^0)$ for film flow on a vertical plate. Without invoking Kármán's approximation they discretized the flow depth and used spectral Fourier expansion in the flow direction. For waves of finite periods they constructed infinitely many branches of solutions which include limit cycles and multiple-hump homoclinic orbits, parameterized by the wavenumber and propagation speed of the waves. They discussed evolution processes on the free surface suggested by the stability of these two-dimensional waves in the presence of streamwise and spanwise perturbations. Since these numerical theories demand that the computational domain be finite, no chaotic waves, which are aperiodic by definition, were found.

Most recently, Yu *et al.* (1995) reported a revised second-order boundary layer theory on a plane, and new experiments on a circular cylinder, for vertically falling water films in the range $R = O(\epsilon^{-1})$ and $W_e = O(1)$. In the theory they corrected the leading-order approximation of Sheintuch & Duckler by adding a centripetal force in the transverse momentum equation. The new term was however inserted by assuming that the curvature term in the boundary layer near a curved wall in an infinite fluid is equivalent to the curvature of the film thickness here. This heuristic correction is incomplete in that it discounts other second-order terms. Based on this revision numerical solutions of stationary waves show the eventual predominance of chaotic waves as the propagation speed was varied from the Hopf-bifurcation threshold. Statistical properties of these chaotic waves including the probability distribution of film thickness, the mean wave speed, and the RMS of film thickness were compared with the experimental observations at 2 m below the entrance of the test tube.

(iv) *Numerical solution of the full Navier–Stokes equations*: All of the numerical theories in this category are restricted to relatively small Reynolds numbers. For instance, Bach & Villadsen (1984) treated the transient problem of a vertically falling flows in the range of $2.5 < R < 25$ by solving the Lagrangian form of the Navier–Stokes equations by finite elements. They found stationary solitary waves emerging at large times. Similarly, Kheshgi & Scriven (1987) used finite elements to obtain stationary periodic and solitary waves along a vertical plate only for $R < 10$. Salamon, Armstrong & Brown (1994) also obtained numerical solutions for periodic and solitary waves on a vertical plane, for $R < 20$; their numerical constructions matched favourably with experimental observations by Kapitza & Kapitza (1949) on a vertical cylinder. In com-

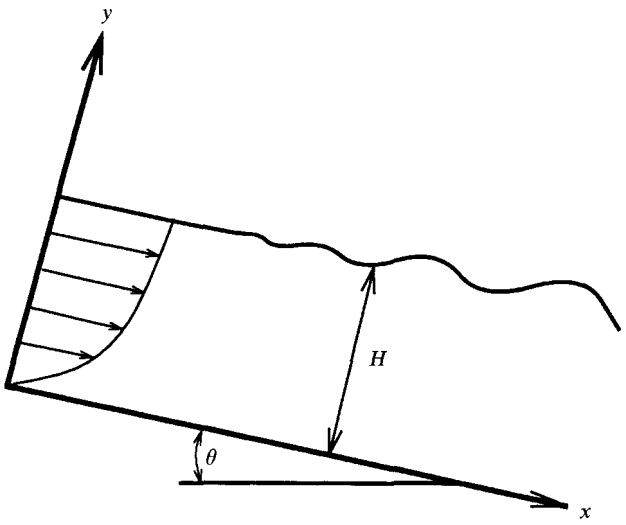

FIGURE 1. Definition sketch.

parison to the leading-order long-wave approximation of Chang *et al.* (1993), their results begin to be different only when the wavenumber ϵ becomes relatively large.

From the brief survey above, it is clear that more information is needed on possible bifurcations that may happen far downstream, especially in the regime of high Reynolds numbers $R = O(\epsilon^{-1})$ and small-to-moderate surface tension $W_e = O(1)$. To examine the dependence of bifurcations on all relevant physical parameters, direct numerical solution of the transient Navier–Stokes equations is of course desirable, but appears to be a formidable task. In this paper we describe an approximate theory accurate to order $O(\epsilon^2)$, without the assumption of hydrostatic pressure. Kármán's momentum integral method is again used. Linearized stability analysis of the uniform primary flow to sinusoidal perturbations is carried out first and the predictions are compared with known measurements of small-amplitude waves in the inception region. We then study permanent wave by analysing the linearized instability of the fixed points and Hopf bifurcation. Finally numerical integration of the dynamical system is carried out to reveal many different bifurcation scenarios, some of which lead to chaos.

2. Approximate governing equations

We consider the two-dimensional flow of a thin layer of an incompressible Newtonian fluid down an inclined plane. Let H denote the flow depth, and θ the angle of inclination of the plane bottom with respect to the horizon. The full range of inclination is allowed so that $0 < \theta \leqslant \pi/2$. A rectangular coordinate system as shown in figure 1 is chosen in which the x-axis coincides with the plane bottom.

With the velocity components denoted by u, v, and pressure by P, the standard Navier–Stokes equations must be supplemented by the following boundary conditions. On the plane sloping bottom, $y = 0$, the velocity components vanish. On the free surface $y = H(x,t)$, the kinematic boundary condition requires that fluid particles can only move tangentially. The dynamic influence of air above is ignored so that tangential and normal stresses must vanish on the free surface. The effect of surface tension is included.

For reference we recall the classical solution for the uniform flow

$$u = \frac{g \sin\theta H_0^2}{2\nu}\left[2\frac{y}{H_0} - \left(\frac{y}{H_0}\right)^2\right], \quad v = 0, \tag{2.1}$$

where g is the gravitational acceleration, ν the kinematic viscosity of the fluid, and H_0 the unperturbed flow depth. The corresponding depth-averaged velocity is

$$u_0 = \frac{g \sin\theta H_0^2}{3\nu} \tag{2.2}$$

and the volume discharge is

$$Q_0 = u_0 H_0. \tag{2.3}$$

For normalization we choose the scales based on the primary flow as follows:

$$x : L, \quad (y, H) : H_0, \quad u : u_0, \quad v : u_0 H_0/L, \quad t : L/u_0, \quad P : \rho u_0^2,$$

where L will be associated with the characteristic wavelength. The film is assumed to be so thin that the ratio $\epsilon \equiv H_0/L$ is small. In normalized variables without distinguishing symbols, the Navier–Stokes equations read

$$u_x + v_y = 0, \tag{2.4}$$

$$u_t + uu_x + vu_y = -P_x + \frac{\sin\theta}{F^2\epsilon} + \frac{\epsilon}{R}u_{xx} + \frac{1}{R\epsilon}u_{yy}, \tag{2.5}$$

$$v_t + uv_x + vv_y = -\frac{1}{\epsilon^2}P_y - \frac{\cos\theta}{F^2\epsilon^2} + \frac{\epsilon}{R}v_{xx} + \frac{1}{R\epsilon}v_{yy}. \tag{2.6}$$

The kinematic boundary condition on $y = H$ is

$$H_t + uH_x = v. \tag{2.7}$$

The stress conditions on the free surface are

$$P + \frac{\epsilon}{R}(u_y H_x - 2v_y) + \frac{W_e \epsilon^2 H_{xx}}{(1 + \epsilon^2 H_x^2)^{3/2}} + \frac{\epsilon^3}{R}v_x H_x = 0, \tag{2.8}$$

$$u_y + R\epsilon P H_x + \epsilon^2(v_x - 2u_x H_x) + \frac{W_e R \epsilon^3 H_{xx} H_x}{(1 + \epsilon^2 H_x^2)^{3/2}} = 0. \tag{2.9}$$

The no-slip boundary condition at the bottom $y = 0$ is

$$u = v = 0 \tag{2.10}$$

In equations (2.5)–(2.9), the dimensionless parameters are

$$\left.\begin{aligned} \epsilon &= H_0/L && \text{ratio of depth to wavelength,} \\ F &= u_0/(gH_0)^{1/2} && \text{Froude number,} \\ R &= u_0 H_0/\nu = g\sin\theta H_0^3/3\nu^2 && \text{Reynolds number,} \\ W_e &= T/\rho H_0 u_0^2 = 9\nu^2 T/\rho g^2 \sin\theta^2 H_0^5 && \text{Weber number,} \end{aligned}\right\} \tag{2.11}$$

where T denotes the surface tension coefficient. Note that F and R are related by $F^2 = R\sin\theta/3$.

In most past works surface tension is assumed to be strong such that $W_e = O(\epsilon^{-2})$, implying that surface tension is of leading-order importance in (2.8). In table 1, we list the physical properties of several common liquids. Based on these values the

	ρ g cm^{-3}	ν cm^2 s^{-1}	T dyne cm^{-1}
Water 15°C	0.999	0.0114	73.5
Glycerine 20°C	1.26	12.16	63
Glycerine–water (50%) 22°C	1.13	0.052	69
Ethyl alcohol 20°C	0.7893	0.0152	23.04
Mercury 20°C	13.5462	0.001147	472

TABLE 1. Physical properties of certain liquids

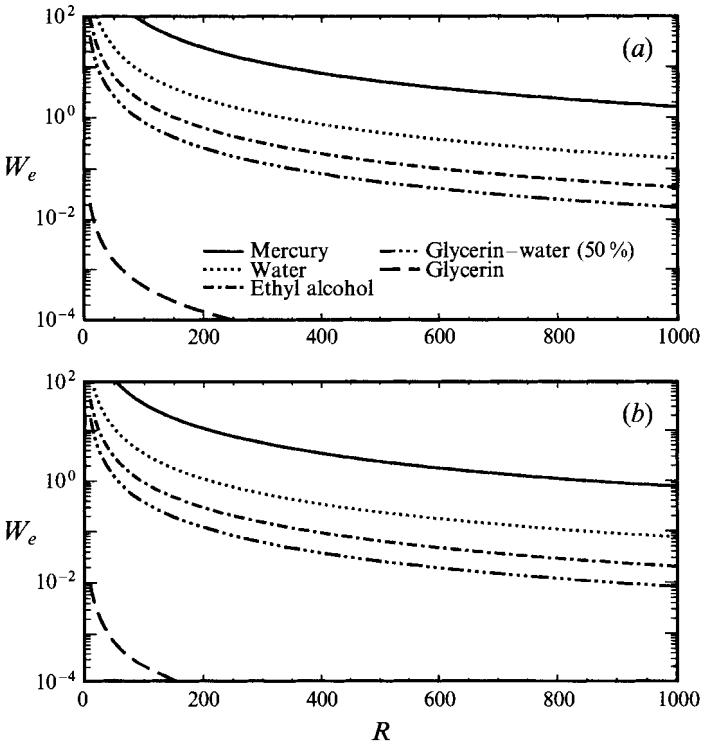

FIGURE 2. Weber number W_e versus Reynolds number R for common fluids listed in table 1. (*a*) $\theta = 1°$, and (*b*) $\theta = 10°$.

Reynolds and Weber numbers are plotted against each other in figure 2 for two different inclinations $\theta = 1°$ and $\theta = 10°$. It is evident that for a wide range of situations, the Reynolds number is large, while the Weber number is small. Therefore in this work we shall assume

$$R = O(1/\epsilon), \quad W_e = O(1). \tag{2.12}$$

Thus our results should complement existing theories on large Reynolds number flows $R = O(\epsilon^{-1})$ with strong surface tension $W = O(\epsilon^{-2})$ (Prokopiou *et al.* 1991; Trifonov & Tsvelodub 1991; Tsvelodub & Trifonov 1992; Chang *et al.* 1993), as well as theories for small Reynolds number flows $R = O(1)$ with either strong surface tension $W_e = O(\epsilon^{-2})$ (Pumir *et al.* 1983; Chang 1986, 1987; Nakaya 1989) or moderate surface tension $W_e = O(1)$ (Nakaya 1975; Chang 1989).

Keeping all terms up to $O(\epsilon^2)$, we get from (2.4)-(2.6),

$$u_x + v_y = 0, \tag{2.13}$$

$$u_t + uu_x + vu_y = -P_x + \frac{3}{R\epsilon} + \frac{\epsilon}{R}u_{xx} + \frac{1}{R\epsilon}u_{yy}, \tag{2.14}$$

$$\epsilon^2(v_t + uv_x + vv_y) = -P_y - \frac{3\cot\theta}{R} + \frac{\epsilon}{R}v_{yy}, \tag{2.15}$$

and from the dynamic boundary conditions (2.8) and (2.9),

$$P + \frac{\epsilon}{R}(u_y H_x - 2v_y) + W_e\epsilon^2 H_{xx} = 0, \tag{2.16}$$

$$u_y + R\epsilon P H_x + \epsilon^2(v_x - 2u_x H_x) + W_e R\epsilon^3 H_{xx} H_x = 0 \tag{2.17}$$

on $y = H$. The kinematic boundary conditions (2.7) and (2.10) remain unchanged.

In their study of high surface tension films, Sheintuch & Duckler (1989) and Prokopiou *et al.* (1991) kept terms of $O(\epsilon^2)$ in the x-momentum equation. However, in the y-momentum equation, they assumed the pressure to be hydrostatic (or uniform if the wall is vertical), which amounts to omitting terms of $O(\epsilon^2)$. For consistency, $O(\epsilon^2)$ terms in all governing equations and boundary conditions should be kept. In Yu *et al.* (1995) these terms were simply replaced by $\rho H_{xx}u^2$, which cannot be theoretically deduced.

Because of the convective nonlinearity, the system (2.13)–(2.17) is highly nonlinear and analytical solution appears infeasible. We follow Kapitza & Kapitza (1949) and apply the approximate momentum integral method of Kármán. As in earlier works by them and by Prokopiou *et al.* (1991), the parabolic velocity profile (2.1), which is the exact solution for the uniform primary flow,

$$u = \frac{3Q}{2H}\left[2\frac{y}{H} - \left(\frac{y}{H}\right)^2\right], \tag{2.18}$$

will be assumed, where $Q(x,t)$, the local flow rate, and $H(x,t)$, the local flow depth, are now regarded as two unknowns. It should be remarked that, despite its success in classical boundary layer theory, the accuracy of Kármán's method is hard to assess *a priori*. We shall only check the result in the linearized limit, as was done in Yu *et al.* (1995) who compared the numerical solution of their approximate equations by assuming a fifth-order polynomial velocity prifile. With (2.18) the two approximate stress boundary conditions (2.16) and (2.17) on the free surface can be further simplified to

$$P = \frac{\epsilon}{R}2v_y - W_e\epsilon^2 H_{xx}, \qquad y = H \tag{2.19}$$

and

$$u_y = \epsilon^2(4u_x H_x - v_x), \qquad y = H. \tag{2.20}$$

The velocity component in the y-direction is readily obtained by integrating the continuity equation (2.13), and applying the no-slip boundary condition (2.10) for v:

$$v = \left(\frac{Q_x}{2H^3} - \frac{3H_x Q}{2H^4}\right)y^3 - \left(\frac{3Q_x}{2H^2} - \frac{3H_x Q}{H^3}\right)y^2, \qquad 0 \leqslant y \leqslant H. \tag{2.21}$$

The pressure distribution in the flow layer can be deduced by integrating the y-momentum equation (2.15) with respect to y from 0 to H, and applying the normal

stress boundary condition (2.19). The result is

$$
\begin{aligned}
P = {} & \frac{3\cot\theta}{R}(H-y) \\
& + \epsilon^2 \left\{ \left(-\frac{QQ_{xx}}{2} + \frac{{Q_x}^2}{2} + \frac{3H_xQQ_x}{20H} + \frac{5H_tQ_x}{8} - \frac{3HQ_{tx}}{8} \right.\right. \\
& \left.\left. + \frac{5H_xQ_t}{8} + \frac{33H_{xx}Q^2}{40H} - \frac{33{H_x}^2Q^2}{2} - \frac{3H_tH_xQ}{2H} + \frac{5H_{tx}Q}{8} \right) \right. \\
& + \left(\frac{-H_tQ_x}{H^3} + \frac{Q_{tx}}{2H^2} - \frac{H_xQ_t}{H^3} + \frac{3H_tH_xQ}{H^4} - \frac{H_{tx}Q}{H^3} \right) y^3 \\
& + \left(\frac{9QQ_{xx}}{8H^4} - \frac{9{Q_x}^2}{8H^4} + \frac{3H_tQ_x}{8H^4} - \frac{Q_{xt}}{8H^3} \right. \\
& \left. + \frac{3H_xQ_t}{8H^4} - \frac{9H_{xx}Q^2}{4H^5} + \frac{9{H_x}^2Q^2}{4H^6} - \frac{3H_tH_xQ}{2H^5} + \frac{3H_{tx}Q}{8H^4} \right) y^4 \\
& + \left(\frac{-3QQ_{xx}}{4H^5} + \frac{3{Q_x}^2}{4H^5} - \frac{3H_xQQ_x}{20H^6} + \frac{9H_{xx}Q^2}{5H^6} - \frac{9{H_x}^2Q^2}{5H^7} \right) y^5 \\
& \left. + \left(\frac{QQ_{xx}}{8H^6} - \frac{{Q_x}^2}{8H^6} - \frac{3H_{xx}Q^2}{8H^7} + \frac{3{H_x}^2Q^2}{8H^8} \right) y^6 \right\} \\
& + \frac{\epsilon}{R} \left\{ \left(\frac{-3Q_x}{2H} + \frac{3H_xQ}{2H^2} \right) + \left(\frac{-3Q_x}{H^2} + \frac{6H_xQ}{H^3} \right) y + \left(\frac{3Q_x}{2H^3} - \frac{9H_xQ}{2H^4} \right) y^2 \right\}. \qquad (2.22)
\end{aligned}
$$

Note that the pressure distribution is hydrostatic only if all terms of $O(\epsilon^2)$ are omitted.

Integrating the approximate equations for continuity and the x-momentum with respect to y over the entire flow depth from $y = 0$ to $y = H$, and making use of the boundary conditions and the assumed velocity profile for u and v, we obtain a pair of equations for Q and H. From the continuity equation (2.13), we have

$$Q_x + H_t = 0. \qquad (2.23)$$

Similarly, from the integrated x-momentum equation (2.14) one gets

$$
\begin{aligned}
& \frac{9QQ_x}{10H} + Q_t - \frac{6H_xQ^2}{5H^2} - \frac{3H_tQ}{2H} + \frac{3\cot\theta HH_x}{R} + \frac{3Q}{H^2R\epsilon} - \frac{3H}{R\epsilon} \\
& + \epsilon^2 \left[-W_eHH_{xxx} - \frac{107HQQ_{xxx}}{280} - \frac{11H^2Q_{txx}}{40} + \frac{87Q^2H_{xxx}}{140} \right. \\
& + \frac{9HQH_{txx}}{20} + \frac{107HQ_xQ_{xx}}{280} - \frac{9H_xQQ_{xx}}{35} + \frac{9HH_tQ_{xx}}{20} \\
& - \frac{HH_xQ_{tx}}{10} + \frac{383H_{xx}QQ_x}{280} + \frac{9HH_{xx}Q_t}{20} - \frac{87H_xH_{xx}Q^2}{70H} \\
& - \frac{21H_tH_{xx}Q}{20} - \frac{3H_{tx}H_xQ}{5} + \frac{71H_x{Q_x}^2}{140} - \frac{87{H_x}^2QQ_x}{70H} \\
& \left. - \frac{3H_tH_xQ_x}{5} + \frac{9{H_x}^2Q_t}{20} + \frac{87{H_x}^3Q^2}{140H^2} \right] \\
& + \frac{\epsilon}{R} \left[-\frac{9Q_{xx}}{2} + \frac{6H_{xx}Q}{H} + \frac{6H_xQ_x}{H} - \frac{6{H_x}^2}{H^2} \right] = 0. \qquad (2.24)
\end{aligned}
$$

Equations (2.23) and (2.24) are two nonlinear partial differential equations describing the temporal and spatial evolution of Q and H.

3. Instability to sinusoidal waves

For checking with experiments and for later reference we sketch the standard analysis on the instability of the uniform flow ($H = Q = 1$) when disturbed by an infinitesimal wavy disturbance. Let h and q denote infinitesimal disturbances from the uniform flow, i.e.

$$H = 1 + h, \quad Q = 1 + q; \tag{3.1}$$

we get upon linearization of (2.23) and (2.24) and elimination of q,

$$\frac{3}{R\epsilon}h_t + \frac{9}{R\epsilon}h_x + \frac{6}{5}h_{xx} + \frac{12}{5}h_{tx} + h_{tt} - \frac{3\cot\theta}{R}h_{xx} - \frac{6\epsilon}{R}h_{xxx} - \frac{9\epsilon}{2R}h_{txx} + \epsilon^2\left(-\frac{87}{140}h_{xxxx} - \frac{11}{40}h_{ttxx} - \frac{233}{280}h_{txxx} + W_e h_{xxxx}\right) = 0. \tag{3.2}$$

Consider a wave-like disturbance

$$h \sim e^{i(x-ct)}. \tag{3.3}$$

This implies that the normalizing length L is chosen to be the reciprocal of the wavenumber in physical dimensions: k^{-1}. Therefore ϵ in (3.2) is just kH_0. By substituting (3.3) into (3.2), a characteristic equation for the complex phase velocity $c = c_r + ic_i$ is found:

$$\left(1 + \frac{11}{40}\epsilon^2\right)c^2 + \left(\frac{3}{R\epsilon}i + \frac{9\epsilon}{2R}i - \frac{12}{5} - \frac{233}{280}\epsilon^2\right)c - \frac{9}{R\epsilon}i - \frac{6\epsilon}{R}i + \frac{6}{5} - \frac{3\cot\theta}{R} + \frac{87}{140}\epsilon^2 - W_e\epsilon^2 = 0. \tag{3.4}$$

Of the two solutions to this quadratic equation with complex coefficients, one corresponds to a stable mode, while the second mode is potentially unstable. The growth rate and phase velocity of the potentially unstable mode can be easily found.

By setting $c_i = 0$ in (3.4) and eliminating c_r from the real and imaginary parts of this complex equation, the threshold for neutral stability is obtained:

$$\epsilon^2\left(11\epsilon^2 + 40\right)R\left[(\cot\theta - R) + \epsilon^2\left(3\cot\theta + \frac{RW_e}{3} - \frac{R}{5}\right) + O(\epsilon^4)\right] = 0. \tag{3.5}$$

On the plane of $(R/\cot\theta)$ versus ϵ, there are three branches of neutral curves. Two of them are trivial: the $(R/\cot\theta)$-axis and the ϵ-axis. The third is given by

$$\frac{R}{\cot\theta} = 1 + \left(\frac{1}{3}W_e + \frac{14}{5}\right)\epsilon^2 + O(\epsilon^4). \tag{3.6}$$

Between the neutral stability curve (3.6) and the $(R/\cot\theta)$-axis, the primary flow is unstable. Surface tension is seen to reduce the region of instability and hence to stabilize the primary flow. In the region of instability, the fastest-growing waves can be found by solving $\partial c_i/\partial\epsilon = 0$. At $\epsilon = 0$, which corresponds to disturbances of infinitely long waves, the condition for instability becomes

$$\frac{\cot\theta}{R} < 1. \tag{3.7}$$

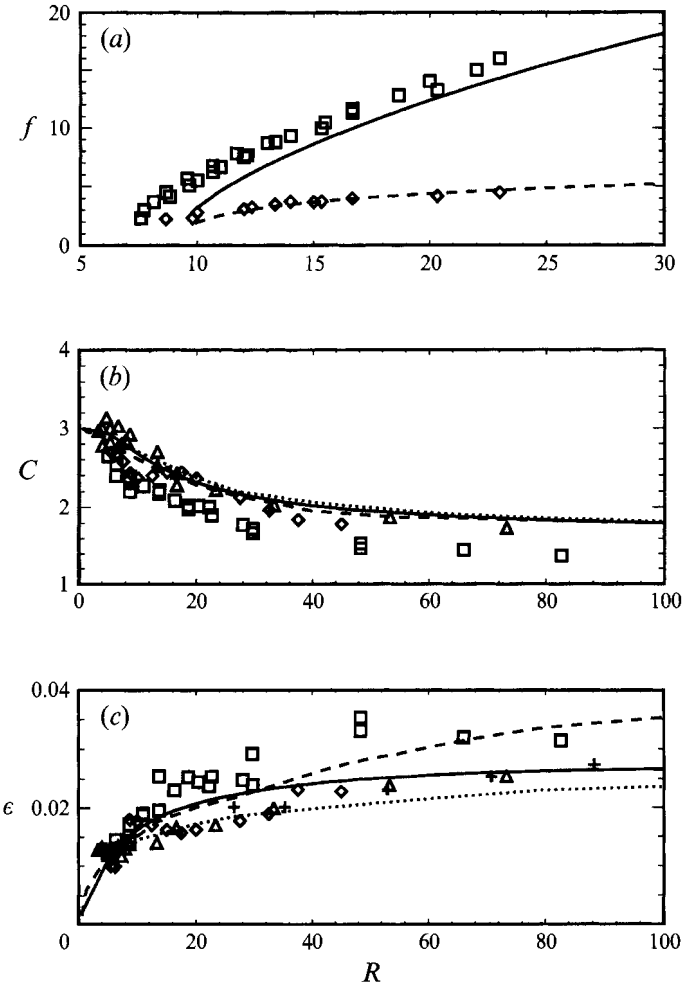

FIGURE 3. Comparison of linear theories with experimental measurement of small-amplitude ripples in the inception region. (*a*) Neutral stability curve (——, theory; □, expt. by Liu & Gollub) and fastest-growing waves (— —, theory; ◇, expt. by Liu & Gollub) for aqueous solutions of glycerine (54 % by weight) down an incline ($\theta = 6.4°$). (*b*) Wavespeeds in the inception region for vertically falling water films: ——, our theory; — —, theory by Pierson & Whitaker; · · ·, theory by Krantz & Goren; □, expt. by Jones & Whitaker; ◇, expt. by Stainthorp & Allen; △, expt. by Strobel & Whitaker. (*c*) Wavenumbers in the inception region for vertically falling water films: +, expt. by Tailby & Portalski. Other symbols as for (*b*).

Throughout this paper we shall call the regime defined by (3.7) the regime of SW(sine-wave)-instability. This threshold value is numerically different from the more accurate result (1.1) of the Orr–Sommerfeld analysis for a small Reynolds number flow. Comparisons of (3.6) and the most unstable waves with one set of experiments by Liu & Gollub (1993) are shown in figure 3(*a*), where for convenience the wavenumber ϵ has been converted to the physical frequency f in Hz. (In dimensional form, the physical frequency f in Hz is related to the wavespeed c and wavelength $1/\epsilon$ by $f = \epsilon c_r/(2\pi H_0/u_0)$). At low Reynolds numbers there is some discrepancy due probably to our momentum integral approximation. The agreement becomes much better for larger R. In figures 3(*b*) and 3(*c*), we also compare

our theoretical predictions (solid curves) of the phase velocity and wavenumber of fastest-growing waves with those experimentally observed near the inception region for vertically falling flows of water at $R < 100$ (Jones & Whitaker 1966; Stainthorp & Allen 1965; Strobel & Whitaker 1969, all for a circular tuble; and Tailby & Portalski 1962 for a plane). Here we follow the custom in the literature and compare the theory for a plane with experiments for a tube of a few centimetres in diameter. Also shown in the figure are approximate solutions from the momentum integral form of the Orr–Sommerfeld equation by Krantz & Goren (1971) and from direct numerical solutions of the Orr–Sommerfeld equation by Pierson & Whitaker (1977). As seen in this figure, the agreement between theoretical predictions and experimental measurement is quite reasonable. Thus the consistent second-order theory with Kármán's approximation is supported by experiments in the parametric domain of interest, at least for small-amplitude disturbances.

In the remainder of this paper only nonlinear stationary waves are considered.

4. The governing equation for stationary waves

It is convenient to transform the approximate system (2.23) and (2.24) to the moving coordinate system defined by $\xi = \epsilon^{-1}(x - ct)$. Equation (2.23) can be used to eliminate the local flow rate Q from (2.24), yielding a third-order ordinary differential equation for the flow depth H:

$$H_{\xi\xi\xi}\left[W_e H^3 - \frac{9c^2}{140}H^4 + \frac{23c(c-1)}{56}H^3 - \frac{87(c-1)^2}{140}H^2\right]$$
$$+H_\xi\left[-\frac{3\cot\theta}{R}H^3 - \frac{c^2}{5}H^2 + \frac{6}{5}(c-1)^2\right] + H_\xi{}^3\left[\frac{c^2}{28}H^2 + \frac{87(c-1)^2}{140}\right]$$
$$+H_\xi H_{\xi\xi}\left[-\frac{c^2}{5}H^3 + \frac{11c(c-1)}{40}H^2 + \frac{87(c-1)^2}{70}H\right]$$
$$+\frac{1}{R}H_{\xi\xi}\left[-\frac{3c}{2}H^2 + 6(c-1)H\right] + \frac{1}{R}6(c-1)H_\xi{}^2 + \frac{3}{R}(H-1)(H^2+H+1-c) = 0. \quad (4.1)$$

We have assumed that the primary flow, $H = 1$ and $Q = 1$, is approached either far upstream, $\xi = -\infty$, or far downstream, $\xi = \infty$. Note that a coordinate renormalization† has been introduced so that the highest-order derivatives appear at the leading order in ϵ. By this normalization, the new horizontal length scale is now the primary flow depth H_0. Consequently the parameter ϵ is no longer present, though $1/R = O(\epsilon)$. By introducing new state variables

$$\overline{H} = H_\xi, \qquad \overline{\overline{H}} = H_{\xi\xi} \quad (4.2)$$

(4.1) can be converted into a three-dimensional dynamical system

$$\frac{dH}{d\xi} = \overline{H}, \qquad \frac{d\overline{H}}{d\xi} = \overline{\overline{H}}, \qquad \frac{d\overline{\overline{H}}}{d\xi} = \frac{F(H,\overline{H},\overline{\overline{H}};\cot\theta/R,R,c)}{D(H;W_e,c)}, \quad (4.3)$$

† If $\eta = x - ct$ is used instead of ξ, it can be shown that the terms associated with $H_{\xi\xi\xi}, H_\xi{}^3, H_\xi H_{\xi\xi}, H_{\xi\xi}, H_\xi{}^2$ are of $O(\epsilon^2)$ higher than the remaining terms in (4.1).

with

$$F \equiv \left[\frac{3\cot\theta}{R}H^3 + \frac{c^2}{5}H^2 - \frac{6}{5}(c-1)^2\right]\overline{H} + \left[\frac{c^2}{28}H^2 + \frac{87}{140}(c-1)^2\right]\overline{H}^3$$
$$+ \left[\frac{c^2}{5}H^3 - \frac{11}{40}c(c-1)H^2 - \frac{87}{70}(c-1)^2H\right]\overline{H}\,\overline{\overline{H}}$$
$$+ \frac{1}{R}\left[(\frac{3c}{2}H^2 - 6(c-1)H)\overline{\overline{H}} + 6(c-1)\overline{H}^2\right] - \frac{3}{R}\left[(H-1)(H^2+H+1-c)\right] \quad (4.4)$$

and

$$D \equiv W_eH^3 - \frac{9}{140}c^2H^4 + \frac{23}{56}c(c-1)H^3 - \frac{87}{140}(c-1)^2H^2. \quad (4.5)$$

Physically H corresponds to the flow depth, $\overline{H}$ to the surface slope, and $\overline{\overline{H}}$ to the surface curvature. Note that F depends on physical parameters c, θ and R, while D depends on c and W_e.

The fixed points can be found by equating the right-hand side of (4.3) to zero, i.e.

$$\overline{H} = 0, \qquad \overline{\overline{H}} = 0, \qquad (H-1)(H^2+H+1-c) = 0, \quad (4.6)$$

which gives two solutions

$$H_I : \quad (H, \overline{H}, \overline{\overline{H}}) = (1, 0, 0) \quad (4.7)$$

and

$$H_{II} : \quad (H, \overline{H}, \overline{\overline{H}}) = \left(\frac{-1+(4c-3)^{1/2}}{2}, 0, 0\right). \quad (4.8)$$

Note that these two fixed points are independent of θ, R and W_e. The first fixed point H_I corresponds to the uniform primary flow. The second fixed point H_{II} varies as a function of c, and remains real and positive only for $c > 1$. This second uniform flow cannot exist by itself for all ξ, and can only be an asymptotic part of a non-uniform profile advancing at the speed $c > 1$. At $c = 3$, H_I and H_{II} cross each other, suggesting a transcritical bifurcation at which the two fixed points exchange their stability properties. Since c alone determines the number of fixed points in (4.3), it will be treaterd as the bifurcation parameter for chosen values of other physical parameters.

5. Singular planes in the phase space

One type of solution that can be of interest is a heteroclinic orbit connecting the two fixed points in the three-dimensional phase space $(H, \overline{H}, \overline{\overline{H}})$. For this to be possible the upstream fixed point must be unstable and the downstream fixed point stable. Moreover, there must be no singularity separating the fixed points in the phase space. At the present order of approximation, singularities exist when the coefficient of $H_{\xi\xi\xi}$ in (4.1) vanishes; or, equivalently, at the zeros of the denominator D in (4.5). In principle these singularities can be removed by extending the approximtion to a higher order, or by avoiding stationary waves and solving initial-boundary value problems numerically. We shall however identify the singularities and examine the consequences of our approximation away from them. Since D involves only one state variable H, these singularities are infinite planes normal to the H-axis in the phase

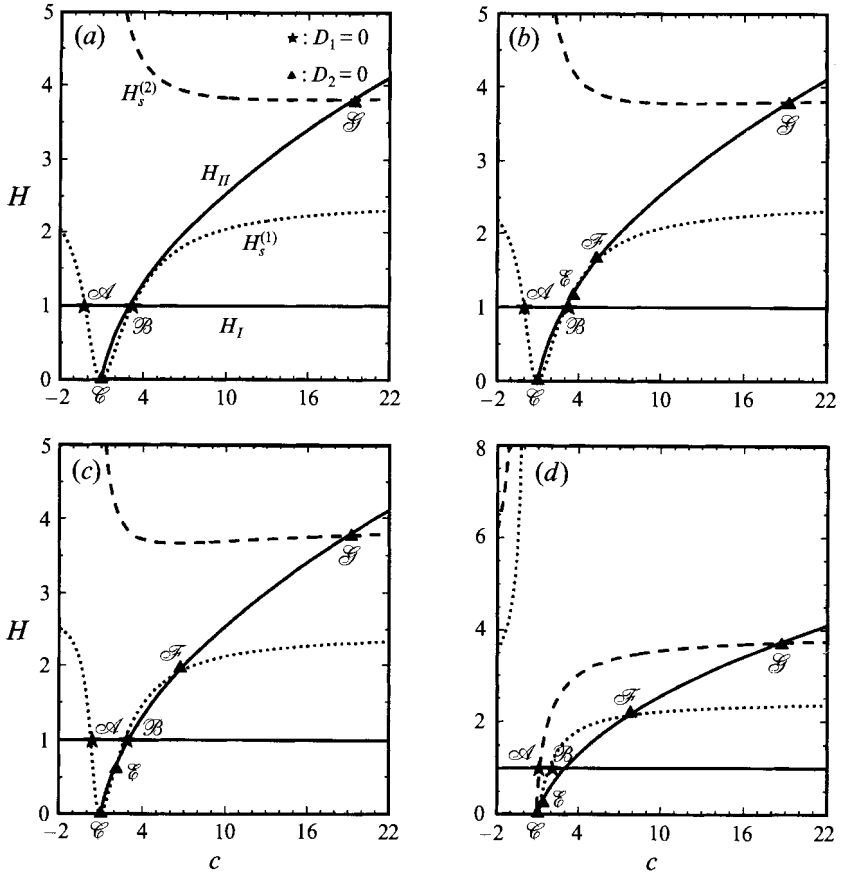

FIGURE 4. Singular planes, $H_s^{(1)}$ and $H_s^{(2)}$, and two fixed points, H_I and H_{II}, versus c. (*a*) $W_e = 0.8$, (*b*) $W_e = 0.65$, (*c*) $W_e = 0.4$, and (*d*) $W_e = 0.025$.

space. One of these planes is simply $H_s^{(0)} = 0$, corresponding physically to a dry bed. Two others depend only on the physical parameters c and W_e:

$$\left.\begin{matrix} H_s^{(1)} \\ H_s^{(2)} \end{matrix}\right\} = \frac{\left[W_e + 23c(c-1)/56\right] \pm \left\{\left[W_e + 23\,(c-1)\,c/56\right]^2 - 783\,(c-1)^2\,c^2/4900\right\}^{1/2}}{(9/70)\,c^2}. \tag{5.1}$$

In figure 4 typical curves of $H_s^{(1)}$ (dotted lines) and $H_s^{(2)}$ (long-dashed lines) are plotted as functions of c, for several sample values of W_e. Curves representing the two fixed points, H_I and H_{II}, versus c are also shown. From the marked points of intersection where the singularity coincides with either one of the two fixed points, the range of c over which the two fixed points lie on the same side of the singular plane in phase space can be delineated. Thus for a large enough W_e, say $W_e = 0.8$, the range of c for the likely occurrence of smooth heteroclinic orbits lies between $\mathscr{C}$ (where $c = 1$) and $\mathscr{B}$ (see figure 4*a*). For a slightly smaller W_e (=0.65), there are two such ranges of interest including $\mathscr{C} - \mathscr{B}$ and $\mathscr{E} - \mathscr{F}$ (see figure 4*b*). For a still smaller W_e(=0.4) (see figure 4*c*), the ranges are $\mathscr{C} - \mathscr{E}$ and $\mathscr{B} - \mathscr{F}$. For a very small W_e (=0.025) (see figure 4*d*), there is only one such range in $\mathscr{B} - \mathscr{F}$.

In the W_e versus c plane the parameter regions where none of the singular planes intrude between H_I and H_{II} in the phase space can be found from the trajectories of

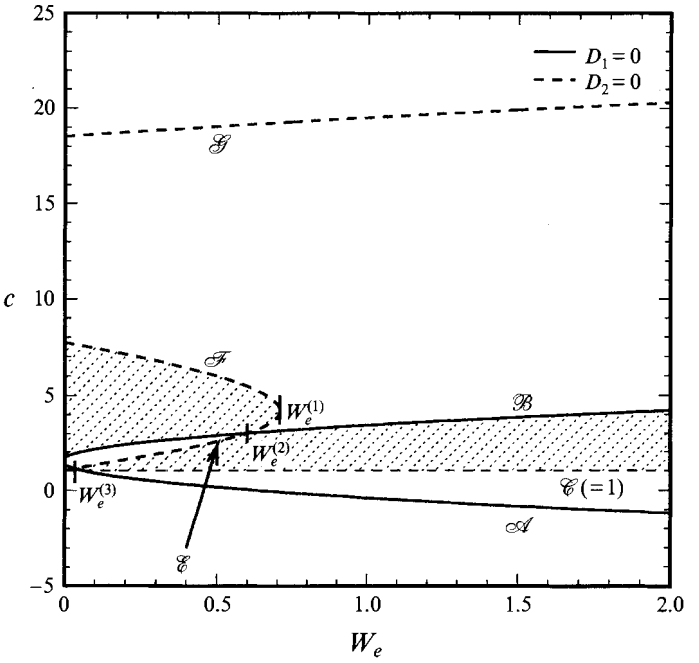

FIGURE 5. Singularity boundaries in the W_e versus c plane, where $\mathscr{A}$ and $\mathscr{B}$ are for H_I, and $\mathscr{C}$, $\mathscr{E}$, $\mathscr{F}$ and $\mathscr{G}$ are for H_{II}. In the shaded regions heteroclinic orbits are possible.

the intersection points between H_I and $H_s^{(1)}$ (or $H_s^{(2)}$), and between H_{II} and $H_s^{(1)}$ (or $H_s^{(2)}$). Such trajectories, which constitute the boundaries of the zones of interest, are found by substituting the fixed point formulas of H_I and H_{II}, i.e. (4.7) and (4.8), into (4.5). Specifically for the first fixed point H_I, the trajectory is given by $D_1(c, W_e) = 0$, where

$$D_1(c, W_e) \equiv W_e - \frac{11}{40}c^2 + \frac{233}{280}c - \frac{87}{140}. \tag{5.2}$$

This is represented by two singularity branches $\mathscr{A}$ and $\mathscr{B}$ of a parabola in the W_e versus c plane as shown by the solid curve in figure 5. Similarly, for the second fixed point H_{II}, the trajectory is given by $D_2(c, W_e) = 0$, where

$$\begin{aligned} D_2(c, W_e) \equiv{}& W_e\left(c(4c-3)^{1/2} - 3c + 2\right) \\ &+ (4c-3)^{1/2}\left(\frac{151}{280}c^3 + \frac{41}{280}c^2 - \frac{87}{70}c + \frac{87}{140}\right) \\ &- \frac{9}{70}c^4 - \frac{99}{40}c^3 + \frac{209}{40}c^2 - \frac{463}{140}c + \frac{87}{140}, \end{aligned} \tag{5.3}$$

which gives rise to four singularity branches $\mathscr{C}$, $\mathscr{E}$, $\mathscr{F}$ and $\mathscr{G}$ as represented by the long-dashed curves in figure 5. In accordance with figure 4, the parameter regions in the W_e versus c plane where the singular planes do not lie between the two fixed points are shaded in figure 5. As W_e decreases towards zero, there are three points of intersection of these singularity branches: $W_e^{(1)}(\approx 0.7072)$ where the singularity branches $\mathscr{E}$ and $\mathscr{F}$ coalesce, $W_e^{(2)}(= 0.6)$ where the singularity branches $\mathscr{B}$ and $\mathscr{E}$ intersect and $W_e^{(3)}(\approx 0.03515)$ where the singularity branches $\mathscr{A}$ and $\mathscr{E}$ intersect. These points divide the W_e line into four regions. The last region is too small to be

of practical interest; in any event to consider such cases of small surface tension one would need to include other higher-order terms so far neglected in our theory.

We now examine the linearized instability of two fixed points H_I and H_{II} in each range of W_e.

6. The eigenvalue equation for fixed-point stability

Let

$$\boldsymbol{H} = \boldsymbol{H}^* + \boldsymbol{h}$$

where $\boldsymbol{H}^*$ represents a fixed point and $\boldsymbol{h}$ the perturbation. Upon linearization of (4.3) for infinitesimal $\boldsymbol{h}$, we get

$$\frac{\mathrm{d}\boldsymbol{h}}{\mathrm{d}\xi} = \boldsymbol{J}\boldsymbol{h} \quad \text{with} \quad \boldsymbol{J} = \begin{pmatrix} 0 & 1 & 0 \\ 0 & 0 & 1 \\ -\beta_3/R & -\beta_2 & -\beta_1/R \end{pmatrix} \tag{6.1}$$

where $\boldsymbol{J}$ is the Jacobian matrix. For the first fixed point H_I, the β-coefficients are

$$\beta_1 = \frac{\frac{9}{2}c - 6}{D_1(c, W_e)}, \quad \beta_2 = \frac{c^2 - \frac{12}{5}c + \frac{6}{5} - (3\cot\theta)/R}{D_1(c, W_e)}, \quad \beta_3 = \frac{3(3-c)}{D_1(c, W_e)}, \tag{6.2}$$

where $D_1(c, W_e)$ is given by (5.2). For the second fixed point H_{II}, the β-coefficients are

$$\left.\begin{aligned} \beta_1 &= \frac{\frac{15}{2}c(4c-3)^{1/2} - 6(4c-3)^{1/2} - 3c^2 - \frac{9}{2}c + 6}{D_2(c, W_e)}, \\ \beta_2 &= \frac{\frac{1}{5}c^2(4c-3)^{1/2} - \frac{2}{5}c^3 + \frac{13}{5}c^2 - \frac{24}{5}c + \frac{12}{5} + [(\cot\theta)/R](-3c(4c-3)^{1/2} + 9c - 6)}{D_2(c, W_e)}, \\ \beta_3 &= \frac{3\left[4c - 3 - 3(4c-3)^{1/2}\right]}{D_2(c, W_e)}, \end{aligned}\right\} \tag{6.3}$$

where $D_2(c, W_e)$ is given by (5.3).

The characteristic equation for the eigenvalue λ of the Jacobian matrix $\boldsymbol{J}$ is

$$\lambda^3 + \frac{\beta_1}{R}\lambda^2 + \beta_2\lambda + \frac{\beta_3}{R} = 0 \tag{6.4}$$

whose solutions determine the stability and type of the fixed point. Exact but lengthy formulae are available for the solutions of this cubic equation, but much insight can be gained from the perturbation solutions in terms of the small parameter $R^{-1} = O(\epsilon)$,

$$\lambda_1 = -\frac{1}{R}\frac{\beta_3}{\beta_2} + O(R^{-2}), \qquad \lambda_{2,3} = \frac{1}{R}\frac{\beta_3 - \beta_1\beta_2}{2\beta_2} \pm \mathrm{i}(\beta_2)^{1/2} + O(R^{-2}). \tag{6.5}$$

From the approximate solution (6.5), if $\beta_2 > 0$, λ_2 and λ_3 are complex and the fixed point is a saddle-spiral. If $\beta_2 < 0$, λ_2 and λ_3 are real and the fixed point is a saddle-node. This approximate solution (6.5) is useful unless $\beta_2 \approx 0$, or in the vicinity of a singularity where D_1 or D_2 vanishes. In the former case numerical solution of (6.4) is needed.

7. Hopf-bifurcation thresholds

From (6.4) and (6.5) we can directly search for the Hopf-bifurcation thresholds, which mark the first appearance of limit cycles, or periodic solutions. This threshold occurs when the fixed point possesses a pair of purely imaginary eigenvalues and a negative real eigenvalue. Therefore, the characteristic equation (6.4) must take the form

$$(\lambda^2 + a)(\lambda + b) = 0 \tag{7.1}$$

with both a and b being real and positive. By direct comparison between (6.4) and (7.1), the following conditions for the threshold of the Hopf-bifurcation are obtained:

$$\beta_1\beta_2 = \beta_3, \qquad \beta_1 > 0, \qquad \beta_2 > 0 \tag{7.2}$$

in which the first inequality assures that the real eigenvalue remains negative, while the second assures that a pair of complex-conjugate eigenvalues exist. In view of (6.2) and (6.3) for the β, (7.2) depends only on three parameters, W_e, c and $\cot\theta/R$. Alternatively, we can arrive at (7.2) from the approximate solutions for eigenvalues given by (6.5). Furthermore, for H_I, the first condition of (7.2) correponds to the condition for neutral stability of the primary flow disturbed by infinitesimal waves, as can be readily proved by setting $c_i = 0$ in (3.4). However, it should be cautioned that not every neutral curve gives rise to a Hopf bifurcation, unless the second and third conditions of (7.2) are also satisfiled.

In the regime of SW-stability, $\cot\theta/R > 1$, the inequality conditions in (7.2) are never satisfied. As a result, no Hopf-bifurcation threshold is found for either fixed point. In the regime of SW-instability, $0 \leqslant \cot\theta/R < 1$, we first plot in figure 6 the two curves c_- and c_+ along which $\beta_2 = 0$ for the first and second fixed point respectively. To see the effects of surface tension, we display also the Hopf-bifurcation thresholds corresponding to $\beta_1\beta_2 = \beta_3$ for $W_e = 5$, 0.65, and 0.3. For the first fixed point H_I the Hopf threshold always lies in the range $c_- < c < 3$. On the other hand, for the second fixed point H_{II} the Hopf threshold occurs only in the range $3 < c < c_+$. For a sufficiently large W_e, say 5, the thresholds for both fixed points (long-dashed lines) span the entire regime of SW-instability, $0 \leqslant \cot\theta/R < 1$, and converge towards the point of neutral stability at $\cot\theta/R = 1$ and $c = 3$. On the other hand, for a relatively small Weber number, say 0.65, the threshold of the second fixed point H_{II} breaks into two separated segments: one in the range $0 \leqslant \cot\theta/R \leqslant (\cot\theta/R)''_+$ (≈ 0.590) with the right end falling on the curve c_+, and the other in the range $(\cot\theta/R)'_+ (\approx 0.940) \leqslant \cot\theta/R < 1$ with the left end falling on the curve c_+ and the right end approaching neutral stability (this segment is too close to c_+ to be seen in figure 6*a*). If the Weber number is further decreased to 0.3, there is only one short threshold segment (the dash-dotted curves) for each of the two fixed points with their right ends retreating along either c_- to $(\cot\theta/R)_- \approx 0.546$ or c_+ to $(\cot\theta/R)''_+ \approx 0.219$ away from the point of neutral SW-stability.

The preceding numerical findings for the Hopf-bifurcation thresholds suggest that the Weber number must exceed a certain minimum for a Hopf bifurcation to occur at a fixed $\cot\theta/R$. These minima can be obtained by demanding that the Hopf-bifurcation threshold curve intersects either c_- for the first fixed point H_I or c_+ for the second fixed point H_{II} at each $\cot\theta/R$. Equivalently, we require that the numerator of β_2 vanishes while at the same time $\beta_1\beta_2 = \beta_3$. However, since β_3 is always finite and positive whenever $\beta_2 = 0$, as can be readily proved from (6.2) and (6.3), the denominator of β_2 , which is the common denominator for all the β, must

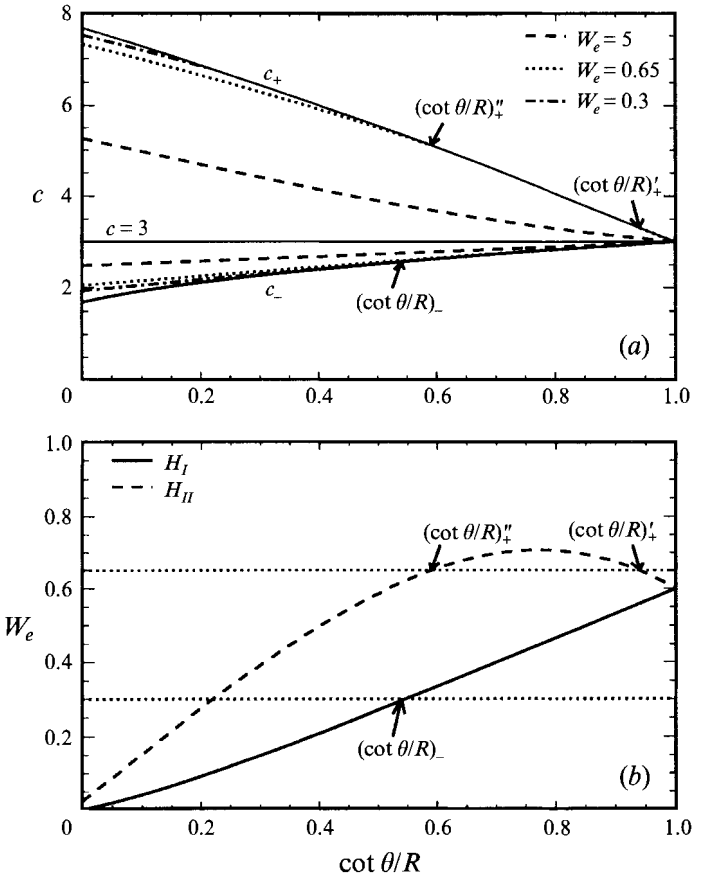

FIGURE 6. (*a*) Hopf-bifurcation thresholds for different Weber numbers. For H_I, the thresholds occur in $c_- < c < 3$; for H_{II}, they exist in $3 < c < c_+$. (*b*) Minumum Weber number for Hopf bifurcations.

be zero. Consequently, by setting both the denominator and numerator of β_2 to zero simultaneously, the minumum Weber number is obtained and plotted as a function of $\cot\theta/R$ in figure 6(*b*), and obviously is a result of the appearance of singularities (see figure 5) in the range $c_- < c < c_+$.

For the first fixed point H_I, the minimum Weber number decreases monotonically from $\frac{3}{5} = 0.6$ at neutral stability, $\cot\theta/R = 1$, towards a small yet non-zero value, 0.00052, at $\cot\theta/R = 0$ for a vertically falling film. Therefore, whenever $W_e > 3/5$, a Hopf-bifurcation threshold can occur in the whole regime of SW-instability. On the other hand, whenever $W_e < 3/5$, say $W_e = 0.3$ shown as the lower horizontal dotted line in figure 6(*b*), only in the regime $0 \leqslant \cot\theta/R \leqslant (\cot\theta/R)_-$ is a Hopf bifurcation possible.

For the second fixed point H_{II}, however, the minumum Weber number curve is no longer monotonic when $W_e \geqslant 3/5 = W_e^{(2)}$ or as long as $0.51742 \leqslant \cot\theta/R \leqslant 1$. The maximum of W_e is just $W_e^{(1)} = 0.7072$, occurring at approximately $\cot\theta/R = 0.75$. Thus whenever $W_e^{(2)} < W_e < W_e^{(1)}$, say $W_e = 0.65$ shown as a horizontal dotted line in figure 6(*b*), there exists a regime, $(\cot\theta/R)''_+ (\approx 0.590) < \cot\theta/R < (\cot\theta/R)'_+ (\approx 0.940)$, in which no Hopf bifurcation can occur, verifying the results for the Hopf-bifurcation thresholds in figure 6(*a*). The minimum Weber number for the second fixed point at $\cot\theta/R = 0$ is calculated to be approximately 0.023.

Since Hopf bifurcations lead to limit cycles, we conclude that a small amount of surface tension must be present in order for periodic solutions to arise from the uniform flow. This is similar to the finding of Lin (1969) who, based on an amplitude equation of Landau Stuart type, showed that for $R = O(1)$ no supercritically stable small-amplitude periodic waves are possible if the Weber number is zero. Benney (1966) reached similar conclusions from a long-wave evolution equation at low Reynolds numbers $R = O(1)$.

8. Stability properties of the fixed points in the parameter plane of $\cot\theta/R$ versus c

In order to help anticipate the variety of numerical solutions to be studied in §9, we shall examine the stability properties of the fixed points together with the positions of the singularities in the parameter space of W_e, R, c, and $\cot\theta/R$. From the analysis so far, the following general conclusions on the properties of the eigenvalues can already be drawn.

(i) As seen from the fixed-point formula (4.7) and (4.8) and the approximate eigenvalue solution (6.5) for λ_1, whenever c crosses 3 for any Weber and Reynolds numbers, and the inclination angle, one of the real eigenvalues of the fixed point changes sign. This is a universal feature of transcritical bifurcation.

(ii) As seen from the characteristic equation (6.4), when a fixed point approaches the singular plane, i.e. $D_1 = 0$ for H_I or $D_2 = 0$ for H_{II}, one of its real eigenvalues approaches positive infinity on one side of the singularity, and negative infinity on the other.

(iii) As seen from (6.5) and (7.2), when the Hopf-bifurcation threshold is crossed by varying c for a fixed W_e and $\cot\theta/R$, the fixed point changes from a stable saddle-spiral ($\lambda_1 < 0, \mathrm{Re}(\lambda_2, \lambda_3) < 0$) to a saddle-spiral with unstable plane focus ($\lambda_1 < 0, \mathrm{Re}(\lambda_2, \lambda_3) > 0$).

In the parameter plane, the boundary separating saddle-spirals from saddle-nodes must correspond to the double root of (6.4), which occurs at

$$\left(\frac{2\beta_1^2}{R^2} - 6\beta_2\right)\left(2\beta_2^2 - \frac{6\beta_1\beta_3}{R^2}\right) - \left(\frac{\beta_1\beta_2}{R} - \frac{9\beta_3}{R}\right)^2 = 0. \tag{8.1}$$

As $R \to \infty$, (8.1) becomes $\beta_2 = 0$, consistent with the perturbation solutions of (6.5).

Except for (8.1), which involves four independent parameters (W_e, θ, R, c), the Hopf-bifurcation thresholds and the singularity boundaries where D_1 for H_I or D_2 for H_{II} vanish are functions of only three parameters (W_e, $\cot\theta/R$, c).

We shall only discuss the eigenvalue behaviour of two fixed points for $W_e > W_e^{(1)}$; similar and lengthier discussions for lower surface tension are presented elsewhere (Lee 1995). From (6.4), the eigenvalues of the fixed points are computed for various domains of the $\cot\theta/R$ versus c plane for a typical Weber number and Reynolds number. The qualitative properties of the eigenvalues are indicated by their locations in the complex plane. For clarity, the two fixed points are separately presented. Based on these calculated eigenvalue properties, we may anticipate two types of continuous orbits in certain parts of the $\cot\theta/R$ versus c plane. The first type is a heteroclinic orbit connecting the two fixed points, either from H_I to H_{II} or from H_{II} to H_I as long as any one of the singular planes does not lie between the two fixed points. The second type is an oscillatory orbit emerging from a limit cycle around the fixed point H_I (or H_{II}) via Hopf bifurcations. As the bifurcation parameter c departs from

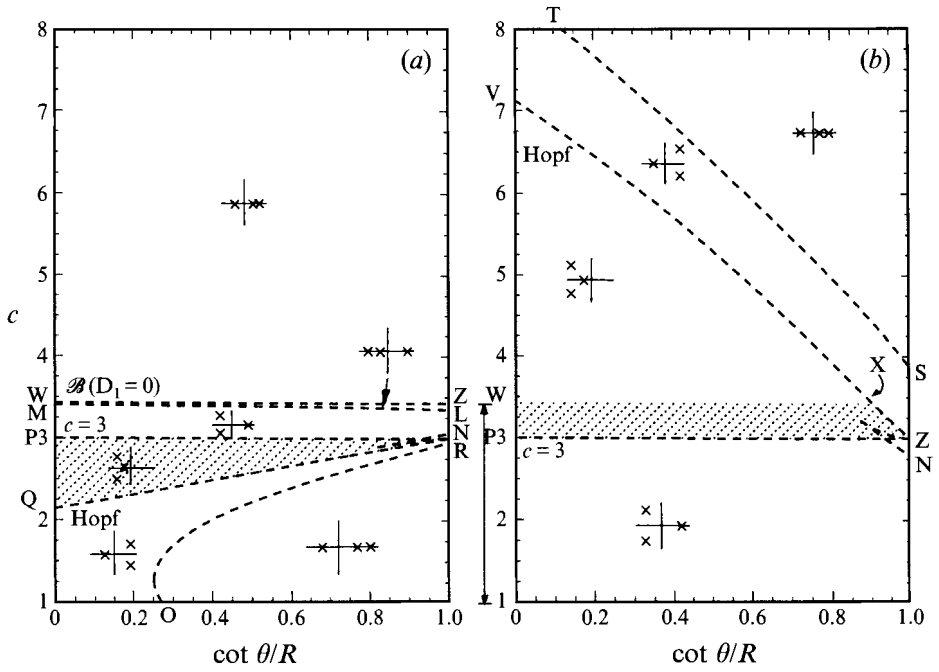

FIGURE 7. Eigenvalue behaviour of fixed points for $W_e = 1$, $R = 1/0.075$. (*a*) H_I, (*b*) H_{II}. The shaded areas are regions of heteroclinic orbits.

the Hopf threshold, the limit cycle bifurcating from H_I (or H_{II}) may grow in both amplitude and wavelength and possibly undergo further bifurcations. The phase orbit may be affected by its proximity to the other fixed point, or pass through the latter to become a homoclinc orbit. To satisfy the initial condition at $\xi \to -\infty$, attractors can be accepted as valid solutions of (4.3) only if their passage to H_I is not blocked by any of the singular planes.

It suffices to discuss the stability properties of two fixed points in the regime of SW-instability $0 \leqslant \cot\theta/R < 1$; in the regime of SW-stability both fixed points are always unstable and do not undergo any Hopf bifurcation. Further, within the SW-instability regime it is only necessary to consider the range of c between $c = 1$ (where H_{II} first emerges) and the singularity branch $\mathscr{G}$ (see figure 5). When c lies above the singularity branch $\mathscr{G}$, neither Hopf bifurcations nor heteroclinic orbits are possible because between the two fixed points, both of which are unstable saddle-nodes according to numerical solutions of (6.4), there are always two singular planes, $H_s^{(1)}$ and $H_s^{(2)}$ (see figure 4). When $c < 1$, there is only one fixed point H_I which does not give rise to any limit cycles through Hopf bifurcation (see figure 6*a*).

In the following, we discuss the implications of eigenvalue properties for $W_e = 1$ and for two Reynolds numbers: $R = 1/0.075 \approx 13.33$ and $R = 100$.

8.1. $W_e = 1$, $R = 1/0.075 \approx 13.33$

The eigenvalue properties of the first and second fixed points are displayed in figures 7(*a*) and 7(*b*), respectively. The neighbourhoods of the point of neutral stability are magnified in figures 8(*a*) and 8(*b*). The Hopf-bifurcation thresholds are shown by QN and VN. The transcritical bifurcation boundary, $c = 3$, is marked by PN. The boundaries dividing saddle-spirals from saddle-nodes are shown for H_I as ML and OR in figure 7(*a*), and IJK and KN in figure 8(*a*), according to (8.1). For H_{II} similar

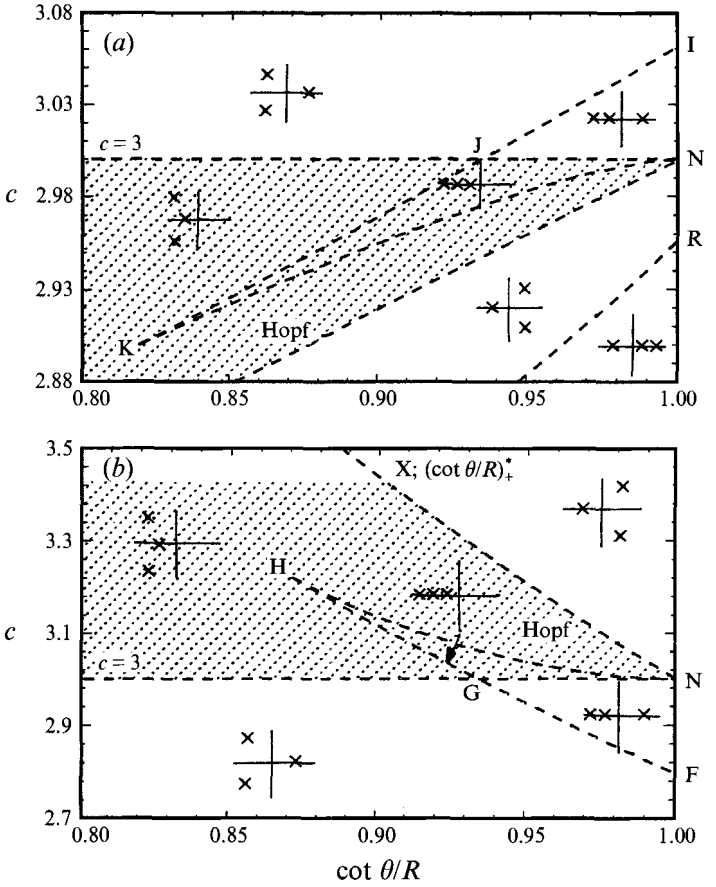

FIGURE 8. (*a*) Enlarged figure 7(*a*) near neutral stability. (*b*) Enlarged figure 7(*b*) near neutral stability.

boundaries are shown by TS in figure 7(*b*), and HGF and HN in figure 8(*b*). The singularity boundary $\mathscr{B}(\approx 3.42760)$ for H_I in figure 7(*a*) is represented by WZ and is horizontal since the Weber number is fixed (see figure 5). Two other singularity boundaries $\mathscr{A}$ and $\mathscr{G}$ are outside the range of the plot (again see figure 5). Determined in accordance with figure 5, the range of c where the singular plane does not intrude in between the two fixed points is marked by the double-headed arrow ($1 < c < c(\mathscr{B})$). It is convenient to discuss the two ranges of wavespeed, $c < 3$ and $c > 3$, separately.

8.1.1. $c < 3$

Consider first the triangular area PNQ, where c lies below $c = 3$ and above the Hopf-bifurcation threshold extending over the whole regime of SW-instability, $0 \leqslant \cot\theta/R < 1$. In this triangle, the first fixed point is either a stable saddle-spiral ($\lambda_1 < 0, \mathrm{Re}(\lambda_2, \lambda_3) < 0$) in region PJKNQ or a stable node ($\lambda_1 < 0, \lambda_2 < 0, \lambda_3 < 0$) in region JKN. In the same triangle H_{II} is either a saddle-spiral with stable plane focus ($\lambda_1 > 0, \mathrm{Re}(\lambda_2, \lambda_3) < 0$) or a saddle-node with stable plane node ($\lambda_1 > 0, \lambda_2 < 0, \lambda_3 < 0$) as shown in figures 7(*b*) and 8(*b*). Since there is no singular plane between the two fixed points, the one-dimensional unstable manifold of H_{II} must intersect the three-dimensional stable manifold of H_I somewhere in the phase space, and a heteroclinic orbit rising from H_{II} to H_I, denoted as $H_{II} \nearrow H_I$, is therefore possible.

Slightly below the Hopf-bifurcation threshold, H_I becomes unstable and may bifurcate supercritically to a limit cycle. If c is decreased further, these limit cycles may undergo more complicated bifurcations. Since H_I and H_{II} remain unstable in the region below the Hopf threshold, no heteroclinic orbit is possible. Nevertheless the limit cycle (or any possible attractor bifurcating from it) is an acceptable continuous solution which can be connected to H_I at $\xi \to -\infty$ and satisfies the initial condition. These speculations will be confirmed by numerical solutions of the nonlinear system (4.3).

8.1.2. $c > 3$

Note that at $\cot\theta/R = (\cot\theta/R)^*_+ \approx 0.9022$ the singularity boundary $\mathscr{B}$ in figure 7(*a*) coincides with the Hopf-bifurcation threshold for H_{II} at X in figure 7(*b*).

In the shaded trapezoidal region WPNX bounded below by $c = 3$ and above partly by the Hopf-bifurcation threshold for H_{II} and partly by the singularity boundary $\mathscr{B}$, H_{II} is a stable saddle-spiral in region WXNHGP (see figures 7*b* and 8*b* together) and a stable node in region NHG (figure 8*b*). As shown in figures 7(*a*) and 8(*a*), H_I is either an unstable saddle-spiral with stable plane focus or a saddle-node with stable plane node in the same trapezoid. Therefore a heteroclinic orbit rising from H_I to H_{II}, denoted as $H_I \nearrow H_{II}$, is possible. In the triangle VWX (figure 7*b*), where two fixed points are separated by the singular plane $H_s^{(1)}$ (see figure 4*a*), no smooth heteroclinic orbit is possible.

In the polygonal region VNST (figure 7*b*), which is bounded below by the Hopf-bifurcation threshold for H_{II} and above by TS, we need only consider the lower triangle XNZ below the singularity boundary $\mathscr{B}$, where attractors, if any exists, bifurcating from H_{II} can be connected to H_I as $\xi \to -\infty$. The region above TS can be disregarded because of the intruding singular plane.

For all $W_e > W_e^{(1)} = 0.7072$ the singularity boundary $\mathscr{B}$ always lies above $c = 3$ (see figure 5). As the Weber number increases, $\mathscr{B}$ in figure 7(*a*) rises with increasing c in the $\cot\theta/R$ versus c plane. Consequently, the regions of possible heteroclinic orbits as well as attractors that can be connected to H_I expand. By demanding the simultaneous satisfaction of both the Hopf-bifurcation threshold conditions (7.2) for H_{II} and the singularity condition (5.2) for H_I at $\cot\theta/R = 0$, we find numerically that, at $W_e \approx 4.3754$, the singularity boundary $\mathscr{B}$ ($c \approx 5.50529$) rises to touch the leftmost end (V) of the Hopf-bifurcation threshold for H_{II} (VN). Therefore, whenever $W_e > 4.3754$, $\mathscr{B}$ lies above VN in the whole regime of SW-instability. Then, any limit cycle newly emerging from H_{II} via Hopf bifurcation can be connected to H_I at $\xi \to -\infty$ to form a continuous orbit. Also a smooth heteroclinic orbit may exist for any c and $\cot\theta/R$ in the corresponding triangular region VPN in figure 7(*b*). However, attractors that arise from further bifurcations of limit cycles cannot form continuous solutions if their speed c exceeds $c(\mathscr{B})$. On the other hand, whenever $W_e < 4.3754$ (e.g. the present case in figure 7*b*), the range of $\cot\theta/R$ for which attractors from H_{II} can be connected to H_I is restricted within $(\cot\theta/R)^*_+ < \cot\theta/R < 1$. The range of possible existence of heteroclinic orbits is also diminished to the corresponding trapezoidal region WPNX in figure 7(*b*).

8.2. $W_e = 1$, $R = 100$

We next raise the Reynolds number to $R = 100$. The eigenvalue behaviour of two fixed points is shown in figures 9(*a*) and 9(*b*). Note that parameter boundaries such as the Hopf-bifurcation thresholds, $c = 3$ and the singularity in the $\cot\theta/R$ versus c plane remain the same as those in the previous case, while the loci of double roots

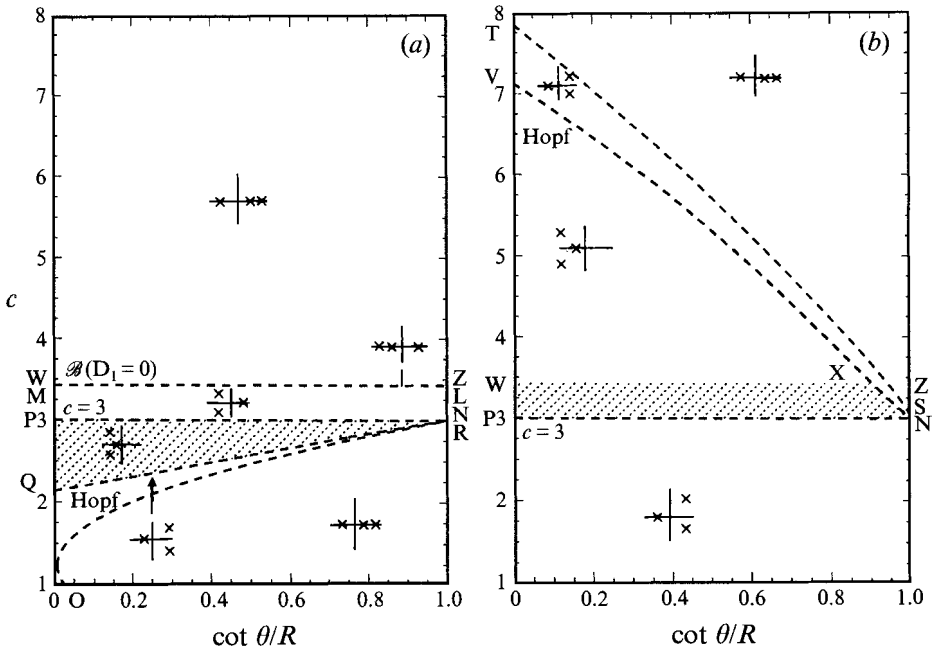

FIGURE 9. Eigenvalue behaviour of fixed points for $W_e = 1$, $R = 100$. (*a*) H_I, (*b*) H_{II}. The shaded areas are regions of heteroclinic orbits.

OR and TS respectively approach c_- and c_+ where $\beta_2 = 0$, while ML becomes almost indistinguishable from the singularity boundary WZ. Note also that, at this larger Reynolds number, the regions of saddle-node or stable node in the neighbourhood of neutral stability shrink in size. Otherwise all conclusions of the previous case of $R = 13.33$ still apply. The qualitative trend continues for still higher Reynolds numbers (up to 1000 by our computation).

Although omitted here, our numerical findings indicate that as the Weber number is reduced (or increased), the region of heteroclinic orbits gradually diminishes (or expands), and so does the span of Hopf-bifurcation thresholds. These phenomena are caused by approaching (or moving away from) singularities and are already evident from figures 4, 5 and 6.

Guided by the linear analysis in this section, we next examine the results of numerical experiments by integrating the nonlinear system (4.3).

9. Numerical study of bifurcation scenarios

Based on the insight gained in the previous section, extensive numerical simulations of the third-order dynamical system (4.3) have been performed for different flow rates with $R = 13.333 = 1/0.075$, 100, and 1000 over a wide range of W_e ($\leqslant 10$). For each set of W_e, R and $\cot\theta$, the propagation speed of the permanent wave c is continuously increased or decreased from the transcritical bifurcation point $c = 3$ to search for either heteroclinic orbits or other nonlinear attractors in phase space. Consistent with the linearized stability analysis of §8, no nonlinear attractor has been found in the regime of SW-stability, $\cot\theta/R \geqslant 1$, for any fixed Weber and Reynolds numbers. This is so because both fixed points are unstable and do not undergo any Hopf bifurcation. Therefore we shall consider only the regime of SW-instability $0 \leqslant (\cot\theta/R) < 1$.

A commercial dynamical systems software, INSITE,† has been used for numerical simulations. For numerical stability, Gear's implicit integration scheme is adopted which allows the user to control the numerical accuracy and time step by specifying the local error bounds. In our simulations, bounds for both absolute and relative error are set between 10^{-9} and 10^{-14} and found to be sufficient.

In the range $0 \leqslant \cot\theta/R < 1$, the predicted existence of heteroclinic connection from linear analysis has been confirmed by integrating the nonlinear system. These orbits indeed leave from the unstable fixed point along the one-dimensional unstable manifold associated with the positive real eigenvalue λ_1^u and approach the stable fixed point along the one-dimensional stable manifold associated with the negative real eigenvalue λ_1^s. As a result the heteroclinc orbits do not undergo oscillations when approaching the stable fixed point. Numerical integration is performed by simply putting the initial phase point in the vicinity of the unstable fixed point. It is only necessary to present sample results for $W_e = 1$, $R = 100$ and $\cot\theta/R = 0.3$. As suggested by the shaded zone F in figure 7(*a*), for any wavespeed c above the Hopf threshold for H_I but below 3.0, the case of $c = 2.5$ is typical. There is a heteroclinic orbit going from H_{II} to H_I ($H_{II} \nearrow H_I$); its phase portrait is shown in figure 10(*a*) and the wave profile in figure 10(*b*). In the phase portrait the first fixed point H_I is marked by a cross ($\times$), and the second fixed point H_{II} by a triangle ($\triangle$). figure 7(*b*) (see the shaded zone WPNX) suggests that for any c above 3.0 but below the singularity boundary $\mathscr{B}(c \approx 4.82032)$, there is then a heteroclinic orbit going from H_I to H_{II} ($H_I \nearrow H_{II}$). The phase portrait and the wave profile are very similar to those in figure 10(*a,b*) and are omitted.

We now direct attention to the much more interesting bifurcation scenarios beyond the Hopf threshold.

When one of the fixed points begins a supercritical Hopf bifurcation, which occurs for the first fixed point H_I (or the second fixed point H_{II}) when c is slightly decreased (or increased) from the Hopf-bifurcation threshold, we put the initial phase point in the neighbourhood of that fixed point. To reduce numerical work, whenever an attractor emerges in the phase space, we relocate the initial phase point next to this attractor and then pursue its subsequent bifurcations. All integrations are carried out for sufficiently long time until the trajectories finally settle down on the attractor. We terminate the simulation at the point where no attractor could be detected when the bifurcation pararmeter c is slightly varied by a magnitude between 10^{-7} and 10^{-9} depending upon the case. Outside the bifurcation range of c where nonlinear attractors exist, the phase trajectories are drawn towards one of the singular planes and lead eventually to infinities (e.g. the region below OR in figures 7*a* and 9*a*; part of the region XNZ in figures 7*b* and 9*b*). This is shown in figure 4, where for $W_e > W_e^{(3)}$, two fixed points are always sandwiched by $H_s^{(0)}$ and $H_s^{(2)}$ in $1 < c < c(\mathscr{G})$. For clarity, the transient start from H_I towards the attractor has been deleted in all the following presentations.

For a specific set of W_e, R and θ, the bifurcation diagram for the permanent wave is constructed by choosing all the local maxima H_m of the time series for the flow depth H as the representative points, which are then plotted against the bifurcation parameter c. In such a diagram, a limit cycle appears as a single representative point, and a period-2 limit cycle as two representative points of differing height, etc. To examine the shape of the attractor in phase space and the wavelength–wavespeed

† INSITE is the acronym for 'Interactive Nonlinear Systems Investigative Tools for Everyone', developed by L.O. Chua & T.S. Parker.

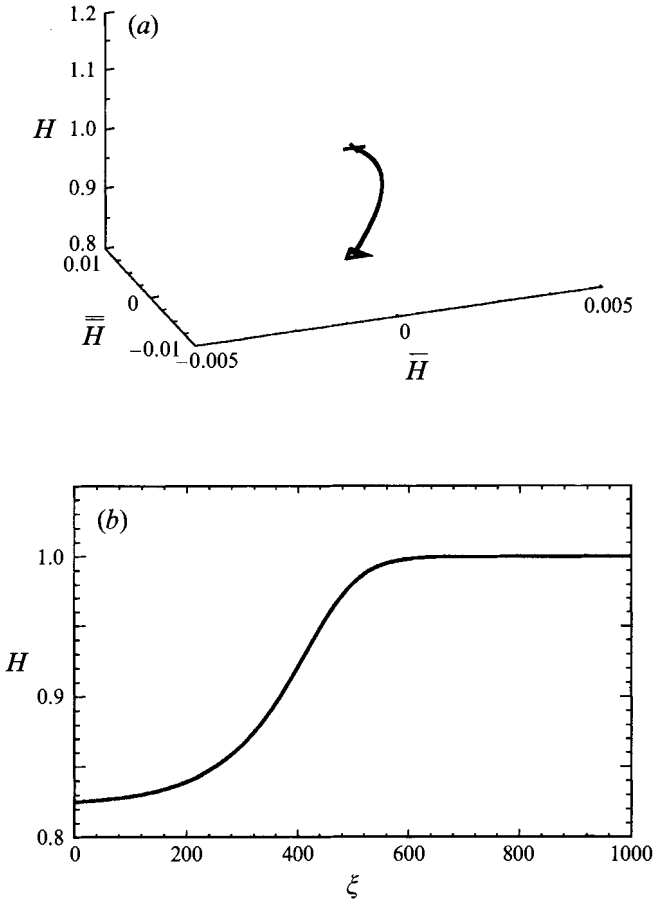

FIGURE 10. Heteroclinic orbit, $H_{II} \nearrow H_I$, for $W_e = 1$, $R = 100$, $\cot\theta/R = 0.3$, and $c = 2.5$. (*a*) Phase trajectory. (*b*) Wave profile.

dispersion relationship during the bifurcation, we shall also present some phase portraits of the attractors and time series of the flow depth for selected values of c.

Bifurcation scenarios beyond the Hopf thresholds are more complicated and strongly dependent upon all physical parameters involved. While numerical experiments have been performed for $R = 13.33$, 100 and 1,000, it is sufficient to present some results for the first two Reynolds numbers.

9.1. *Bifurcations from the primary flow* H_I

9.1.1. *Moderate Reynolds number,* $R = 1/0.075 \approx 13.33$

From extensive studies over a wide range of Weber numbers, $W_e \leqslant 10$, we have uncovered four different bifurcation scenarios: (*a*) *simple homoclinic bifurcations* in which the limit cycle from H_I undergoes an infinite-period bifurcation to become a homoclinic orbit passing through H_{II}; (*b*) *multiple-hump homoclinic bifurcations* in which the limit cycle first undergoes a series of period-doubling before a homoclinic bifurcation takes over which eventually leads to an n-hump ($n \geqslant 1$) homoclinic orbit passing through H_{II}; (*c*) cascades of *period-doubling bifurcations* that lead to chaos; and (*d*) *limit cycles*. We have numerically determined the boundaries separating regimes of different bifurcation scenarios in terms of $\cot\theta/R$ for each W_e; results for

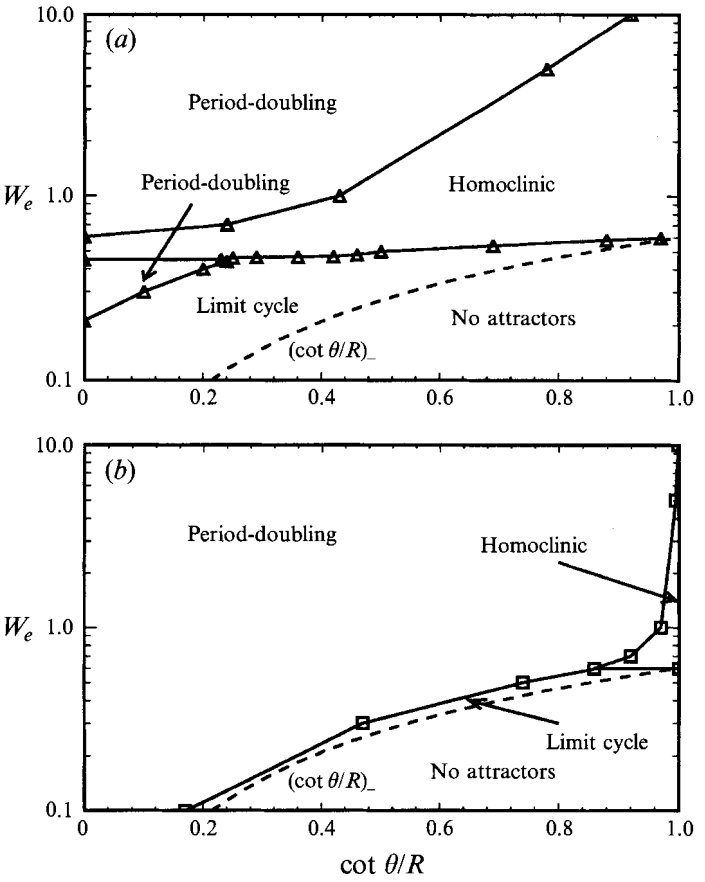

FIGURE 11. Bifurcation scenarios for H_I. (*a*) $R = 1/0.075 \approx 13.33$. (*b*) $R = 100$.

a wide range of $W_e < W_e^{(2)}$ are summarized in figure 11(*a*). In the same plot we also mark the curve of $(\cot\theta/R)_-$ to the right of which no Hopf-bifurcation thresholds and therefore no attractors exist (see figure 6).

When $W_e > W_e^{(2)}(= 0.6)$, where the Hopf-bifurcation threshold extends throughout the entire regime of SW-instability, the limit cycle either undergoes homoclinic bifurcations or period-doubling bifurcations. Homoclinic bifurcations dominate over most range of $\cot\theta/R$ for smaller Weber numbers, whereas period-doublings prevail for larger Weber numbers. When $W_e < W_e^{(2)}$, the Hopf-bifurcation threshold only exists in $0 \leqslant (\cot\theta/R) < (\cot\theta/R)_-$ due to the intrusion of a singular plane in between two fixed points (see figure 4). No homoclinic bifurcation is possible. Instead, in the neighbourhood of $(\cot\theta/R)_-$, only limit cycles survive without further bifurcations. For extremely low surface tension, only limit cycles are possible.

We only present in the following the typical bifurcation sequences for $W_e = 1$ for a set of descending $\cot\theta/R$ from neutral stability (increasing slope).

(*a*) $\cot\theta/R = 0.7$: *Simple homoclinic bifurcation*

Recall that for the first fixed point H_I, the Hopf-bifurcation threshold spans the whole regime of SW-instability, $0 \leqslant \cot\theta/R < 1$ (cf. figures 7*a* and 11*a*). Furthermore, below the Hopf-bifurcation threshold, no singular plane intrudes between H_I and H_{II}. Numerical experiments indicate that in the close neighbourhood of neutral SW-

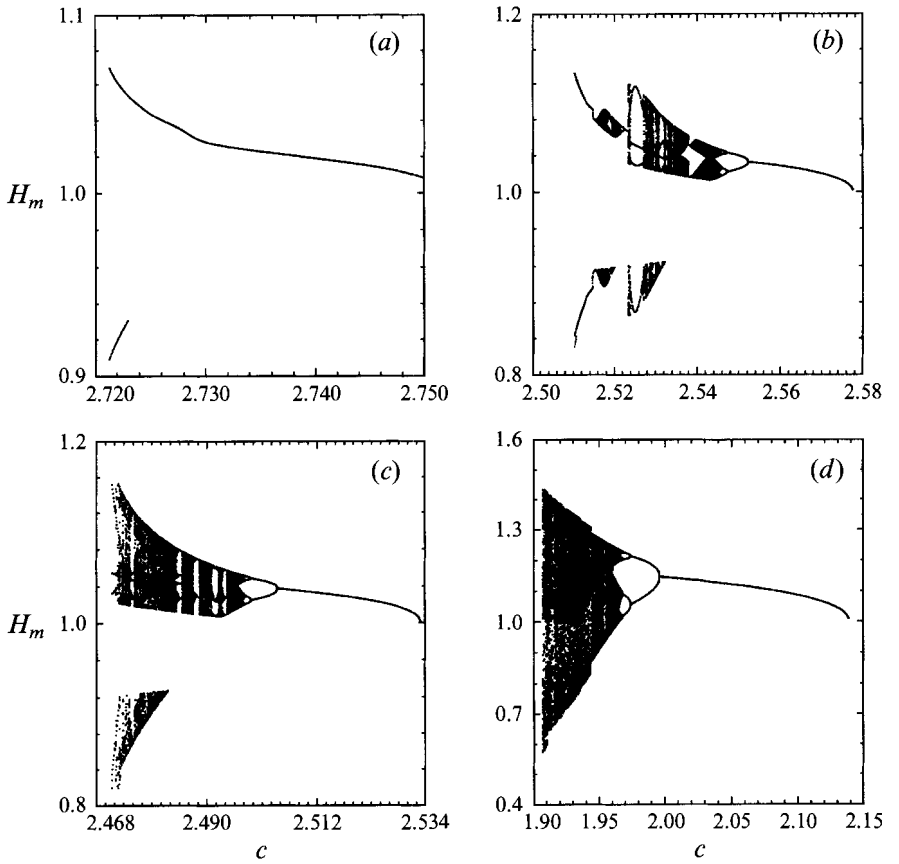

FIGURE 12. Selected bifurcation diagrams for $W_e = 1$, $R = 1/0.075 \approx 13.33$. (*a*) $\cot\theta/R = 0.7$, simple homoclinic bifurcation. (*b*) $\cot\theta/R = 0.5$, period-doublings leading to simple homoclinic bifurcation. (*c*) $\cot\theta/R = 0.45$, three-hump homoclinic orbit emerging in the end. (*d*) $\cot\theta/R = 0$, period-doubling bifurcations leading to chaos.

stability (see figure 8), limit cycles from H_I undergo a homoclinic bifurcation to become a homoclinic orbit passing through H_{II} which is of the saddle-node type. With further reduction of $\cot\theta/R$ away from neutral stability, the homoclinic orbit passes through H_{II} of saddle-spiral type. Strict homoclinicity is difficult to achieve numerically, hence the calculated profile is a train of periodic waves with very long periods. Within each period there is a prominent peak which possesses front-running ripples if H_{II} is a saddle-spiral.

For the case of $\cot\theta/R = 0.7$ under study, the Hopf-bifurcation threshold is approximately at $c = 2.75188$ from (7.2). The bifurcation diagram is shown in figure 12(*a*). Corresponding to the starting (upper) primary branch in figure 12(*a*), the limit cycle increases its amplitude and wavelength as the bifurcation parameter c is reduced. The lower secondary branch in figure 12(*a*), which first appears at approximately $c = 2.72292$, corresponds to small ripples between consecutive wavefronts. Judging from the position of H_{II} (4.8) in phase space, which is a saddle-spiral with a stable plane focus (figure 7), clearly this secondary bifurcation branch arises because the orbit structure of the growing limit cycle is affected by approaching H_{II}. At near-homoclinicity $c = 2.7212292264$ (figure 13*a*), a homoclinic orbit is formed which slowly rises from H_{II}, winds around H_I and then returns to H_{II}. The wave profile

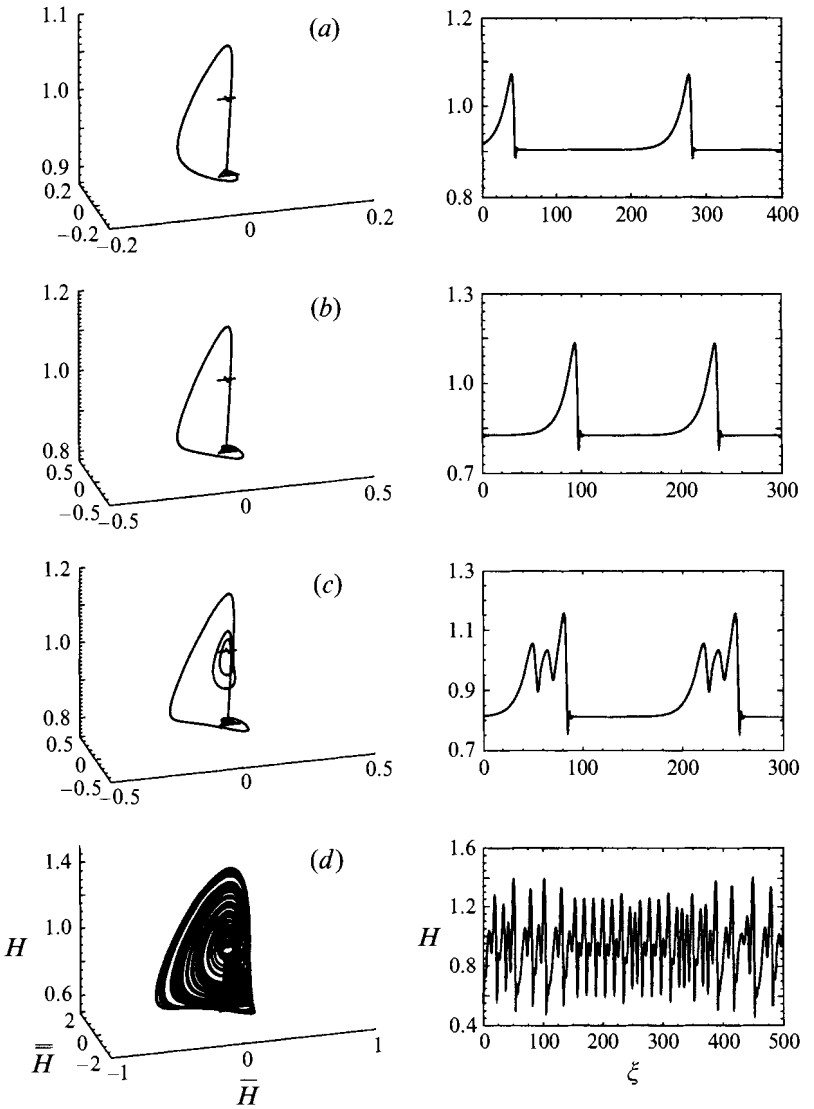

FIGURE 13. Selected phase portraits and corresponding wave profiles near the end of bifurcations for $W_e = 1$, $R = 1/0.075 \approx 13.33$. (*a*) $\cot\theta/R = 0.7$, $c = 2.7212292264$. (*b*) $\cot\theta/R = 0.5$, $c = 2.5102077$. (*c*) $\cot\theta/R = 0.45$, $c = 2.51029995$. (*d*) $\cot\theta/R = 0$, $c = 1.90988$.

is a series of well-separated solitary waves with steep wavefronts and a mild sloping back possessing rippled tails. The profile strongly resembles those observed in the tube experiments of Kapitza & Kapitza (1949) and the plane experiments of Liu & Gollub (1993, 1994). In the numerical experiments, strict homoclinicity with infinite period cannot be achieved, but the trend demonstrated in figure 12(*a*) is clear.

According to the well-known Sil'nikov theorem (1965; see also Wiggins 1990 or Guckenheimer & Holmes 1983) complicated and chaotic dynamics occur in the neighbourhood of a homoclinc orbit passing through a fixed point of saddle-spiral type with stable plane focus, if the magnitude of the real eigenvalue is greater than the magnitude of the real part of the complex eigenvalue pair. From (6.5) the condition

amounts approximately to

$$\beta_3 < -\beta_1\beta_2 \tag{9.1}$$

at the fixed point passes by the homoclinic orbit. In the present case the eigenvalues of H_{II} at near-homoclinicity are $[\lambda_1 = 0.073234, \mathrm{Re}(\lambda_2, \lambda_3) = -0.70333]$, which do not satisfy the Sil'nikov criterion, hence no complex dynamics follows.

(b) $\cot\theta/R = 0.5$: *Period-doublings + simple homoclinic bifurcation*

Further away from the threshold of SW-instability, the bifurcation scenario becomes more complicated. The limit cycle from H_I undergoes cascades of period-doubling bifurcations before finally yielding to a simple homoclinic bifurcation with a one-hump homoclinic orbit passing through H_{II}. From (7.2), the Hopf-bifurcation threshold is estimated to be $c = 2.57755$. The bifurcation diagram is shown in figure 12(b). The phase portrait of the final attractors and the corresponding wave profile are shown in figure 13(b).

As seen in figure 12(b), as c decreases from the Hopf-bifurcation threshold, the limit cycle from H_I first undergoes a series of period-doubling bifurcations to become a chaotic attractor. Then through another series of period-halving bifurcations, the chaotic attractor evolves into a periodic attractor once again. In fact, there are many cascades of such period-doubling and period-halving bifurcations occurring repeatedly in different ranges of c to create intermittant chaotic zones. Embedded within the chaotic zones are some periodic windows created by period-halving bifurcations which contain periodic orbits of odd or even periods. Some of these windows are evident, such as the period-3 limit cycle in the interval $2.523 < c < 2.528$. These phenomena are typical of many nonlinear dynamical systems (e.g. the Lorenz and Rössler systems). In addition, the isolated secondary bifurcation branches in the lower part of the bifurcation diagram figure 12(b), which correspond to the small ripples in the wave profile, also undergo their own complicated period-doubling bifurcations. Only near the end of the bifurcation sequence (roughly when $c < 2.544$), is there a period-1 limit cycle emerging from a period-halving bifurcation, yielding a one-hump homoclinic orbit. At near-homoclinicity $c = 2.5102077$ (figure 13b), the attractor passess through H_{II} at which the eigenvalues are $[\lambda_1 = 0.0970039, \mathrm{Re}(\lambda_2, \lambda_3) = -0.691272]$. Sil'nikov's criterion is again not satisfied.

(c) $\cot\theta/R = 0.45$: *Multiple-hump homoclinic bifurcations*

As the value of $\cot\theta/R$ is further decreased, the limit cycle from H_I eventually undergoes a homoclinic bifurcation which leads to a multiple-hump homoclinic orbit passing through H_{II}. Such bifurcations are always preceded by complicated cascades of period-doubling and period-halving bifurcations. Indeed a period-n (with $n > 1$) limit cycle must appear first before it can undergo a homoclinic bifurcation and become an n-hump homoclinic orbit. In the following, we present just one such case for $\cot\theta/R = 0.45$ which leads to a three-hump homoclinic orbit. We have also found that at $\cot\theta/R = 0.44$ a six-hump homoclinic orbit results; details are omitted here.

Figure 12(c) shows the bifurcation diagram, where the Hopf-bifurcation threshold is estimated to be $c = 2.53314$. Similar to the previous case shown in figure 12(b), numerous periodic windows are sandwiched by sequences of period-doubling and period-halving bifurcations. The phase portrait of the final attractor during the bifurcation and its corresponding wave profile are shown in figure 13(c). At near-homoclinicity $c = 2.51029995$, there emerges a three-hump homoclinic orbit passing through H_{II}, which is still a saddle-spiral with stable plane focus. The eigenvalues

of H_{II} at near-homoclinicity are $[\lambda_1 = 0.100266, \mathrm{Re}(\lambda_2, \lambda_3) = -0.689083]$, which does not satisfy Sil'nikov's criterion.

Multiple-hump homoclinic orbits were first discovered for film flows at low Reynolds numbers $R = O(1)$ and large surface tension $W_e = O(\epsilon^{-2})$ by Pumir *et al.* (1983) for flows on an inclined plane and Nakaya (1989) for vertically falling flows, who numerically constructed such waves in the long-wave equation of Benney (1966). Chang *et al.* (1993) also presented such solutions in the case when both Reynolds and Weber numbers are large ($R = O(\epsilon^{-1}), W_e = O(\epsilon^{-2})$).

(d) $\cot\theta/R = 0$: *Period-doubling bifurcations towards chaos*

As the value of $\cot\theta/R$ is further decreased from 0.44 (see figure 11a), no homoclinic bifurcations for the limit cycles from H_I can be found throughout the bifurcation processes. Instead, period-doubling bifurcations leading to a chaoic attractor become the dominant scenario. This is not surprising, since from §3 a smaller $\cot\theta/R$ corresponds to a more unstable regime, where higher growth rates of perturbations quickly contribute to the chaotic appearance of the free surface. However, as evidenced from previous cases, the detail of each bifurcation process at a fixed $\cot\theta/R$ has its own peculiar characteristics. With $\cot\theta/R$ further reduced, approach from period-doubling to chaos is more rapid. For brevity, we only present results for the special case of $\cot\theta/R = 0$ (vertical wall) here.

We show in figure 12(d) the bifurcation diagram; the phase portrait of the final attractor and its corresponding wave profile are shown in figure 13(d). The Hopf-bifurcation threshold is estimated to be $c = 2.1385$. As the bifurcation unfolds, the representative points grow in both number and range. Intermittent windows can still be seen in the bifurcation diagram. The fixed point H_I is totally immersed in the chaotic trajectories (see figure 13d).

We next turn to $R = 100$.

9.1.2. *Fairly large Reynolds number: $R = 100$*

As the Reynolds number is increased to $R = 100$, period-doubling bifurcations rapidly expand to most of the range of $\cot\theta/R$ where a Hopf bifurcation exists. For instance, at $W_e = 1$ and $R = 100$, we numerically determine that the homoclinic regime resides only within a narrow strip $0.97 < \cot\theta/R < 1$, whereas the period-doubling regime extends over $0 \leqslant \cot\theta/R < 0.97$. For a wide range of W_e the bifurcation scenarios are summarized in figure 11(b). In comparion to the previous case for lower Reynolds number (cf. figure 11a), the homoclinic regime has retreated to the close neighbourhood of neutral stability in $W_e > W_e^{(2)}$, while the limit-cycle regime has also diminished towards the vicinity of $(\cot\theta/R)_-$ in $W_e < W_e^{(2)}$. These trends continue as the Reynolds number is increased further to $R = 1000$.

We next turn to the bifurcation scenarios of the limit cycles from H_{II}.

9.2. *Bifurcations from H_{II}*

For H_{II}, we need only consider $W_e > W_e^{(2)} (= 0.6)$, since otherwise the passage from H_{II} to H_I is blocked by a singular plane as H_{II} undergoes a Hopf bifurcation (see figure 4). Again, we discuss $R = 1/0.075 \approx 13.33$ and $R = 100$ separately.

9.2.1. *Moderate Reynolds number $R = 1/0.075 \approx 13.33$*

According to figure 7(b), only for $(\cot\theta/R)_+^* < \cot\theta/R < 1$, and for c lying below the singularity boundary $\mathscr{B}$, can any attractors bifurcating from H_{II} be connected smoothly to H_I and constitute acceptable solutions to (4.3). Recall that $(\cot\theta/R)_+^*$

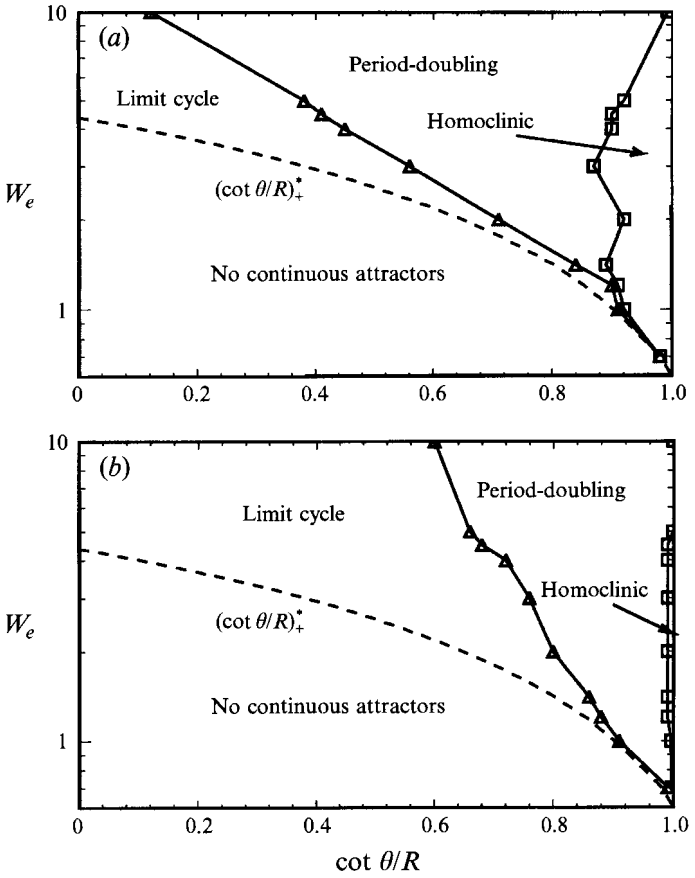

FIGURE 14. Bifurcation scenarios for H_{II}. (*a*) $R = 1/0.075 \approx 13.33$. (*b*) $R = 100$.

depends only on W_e, but not on R. As W_e is increased, the range of $\cot\theta/R$ for acceptable solutions quickly expands.

For $R \approx 13.33$ and $W_e^{(2)}(= 0.6) < W_e \leqslant 10$, figure 14(*a*) summarizes the different bifurcation scenarios in the W_e versus $\cot\theta/R$ plane; $(\cot\theta/R)_+^*$ is also shown as a dashed curve. As in the case of H_I, there are three distinct bifurcation regimes: homoclinic, period-doubling and limit cycles. Homoclinic bifurcations here lead to homoclinic orbits passing through H_I. However, unlike H_I in figure 11, H_{II} in the limit-cycle regime still undergoes period-doubling bifurcations leading to chaos. Nonetheless, among all these attractors, only the limit cycles with small enough propagation speed, $c < c(\mathscr{B})$, can be connected to H_I and constitute acceptable solutions. From figure 14(*a*), as the Weber number is increased, period-doubling bifurcations prevail over the homoclinic and limit-cycle regimes. Conversely, as the Weber number is decreased towards $W_e^{(2)}(= 0.6)$, the influence of the singularity $(\cot\theta/R)_+^*$ gradually becomes evident until eventually H_{II} cannot be connected to H_I in the whole regime of SW-instability; therefore no continuous solutions are possible.

We next present some typical results for $W_e = 5$. Solutions connecting H_I to attractors emanating from H_{II} exist in the whole regime of SW-instability, $0 \leqslant \cot\theta/R < 1$. We find that the homoclinic regime resides in $0.92 < \cot\theta/R < 1$; the period-doubling regime exists in $0.38 < \cot\theta/R < 0.92$; and the limit-cycle regime is

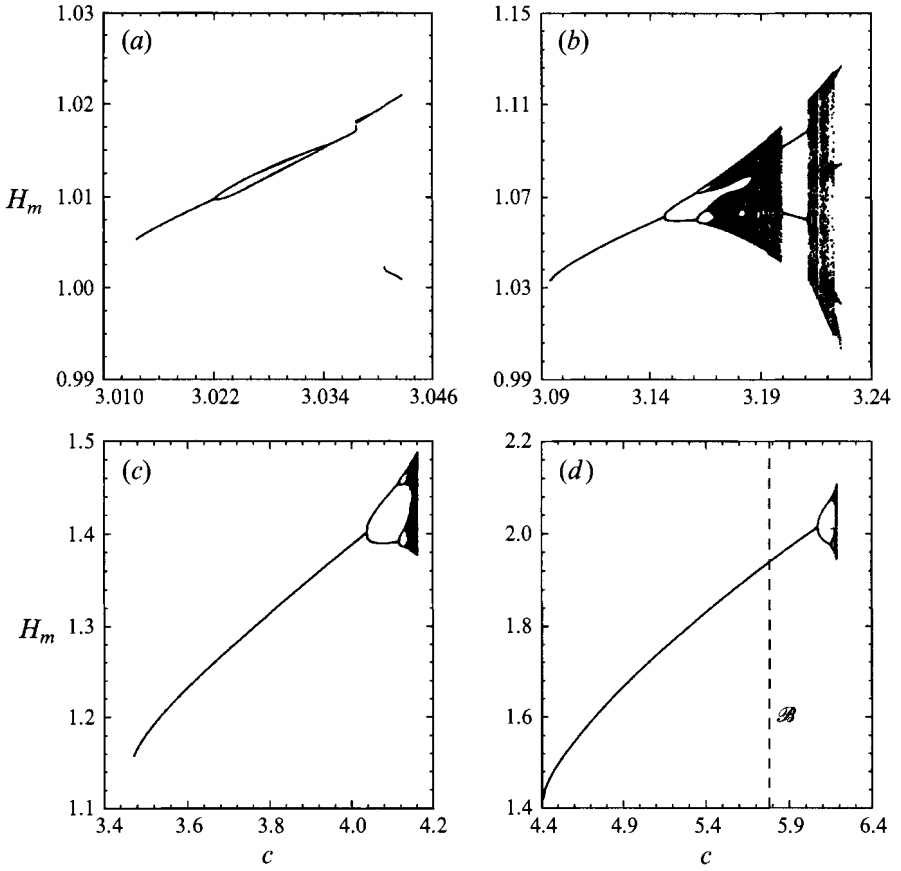

FIGURE 15. Selected bifurcation diagrams for $W_e = 5$, $R = 1/0.075 \approx 13.33$. (*a*) $\cot\theta/R = 0.99$, simple homoclinic bifurcation leading to a one-hump homoclinic orbit. (*b*) $\cot\theta/R = 0.93$, period-doublings leading to two-hump homoclinic orbit. (*c*) $\cot\theta/R = 0.7$, period-doublings leading to chaos. (*d*) $\cot\theta/R = 0.3$, limit cycles

in $0 \leqslant \cot\theta/R < 0.38$. Shown in figure 15 are several typical bifurcation diagrams of the three different bifurcation scenarios. In figure 15(*a*) where $\cot\theta/R = 0.99$, the limit cycle from H_{II} undergoes a sequence of period-doublings and period-halvings, before a sudden jump that eventually settles to a one-hump homoclinic orbit passing through H_I. Since the eigenvalues at H_I are such that $[\lambda_1 = 0.043838, \mathrm{Re}\,(\lambda_2, \lambda_3) = -0.088011]$, the Sil'nikov criteron is not satisfied. In figure 15(*b*) where $\cot\theta/R = 0.93$, period-doubling bifurcations precede a two-hump homoclinic bifurcation. Figure 15(c) where $\cot\theta/R = 0.7$ shows chaos following period-doubling bifurcations. In figure 15(*d*) where $\cot\theta/R = 0.3$, the limit cycle from H_{II} obviously undergoes period-doubling bifurcations. However, solutions connecting to H_I occur only in $c < c(\mathscr{B})$ $(c \approx 5.78)$ which are only limit cycles. The phase portraits and wave profiles can be qualitatively inferred by analogy with figure 13.

9.2.2. *Fairly large Reynolds number, $R = 100$*

For brevity, we only display the computed boundaries of bifurcation scenarios in figure 14(*b*). In comparision with figure 14(*a*) for the lower $R = 1/0.075 \approx 13.33$, all bifurcation-scenario boundaries shift towards neutral stability. The homoclinic regime is now negligibly small. The extent of the limit-cycle regime also grows, indicating that

as the Reynolds number increases, the bifurcation range of c for nonlinear attractors to exist also increases. These trends continue as R is further increased to $R = 1000$.

10. Comparison with experiments

As pointed out before, the majority of past experiments on finite-amplitude waves concern falling water films along vertical circular cylinders of limited length. For example periodic waves were recorded by Stainthorp & Batt (1967) in the top 4 to 58 cm of a 76 cm long tube, and by Jones & Whitaker (1966) in the top 6 to 8 cm of a 45 cm long tube. Since these observations may still be in the transient stage of development while our theory corresponds to the asympotic state of large time or fetch for films on a plane, definitive comparisions are difficult. Furthermore, in these experiments surface tension is rather strong (usually $W_e > 20$). With these reservations we now compare our calculations for each R, the highest period-1 waves taken at the threshold where the first fixed point H_1 bifurcates to a period-2 limit cycle (represented as the solid curve in figure 16). Also included for comparision are the theoretical predictions by Lee (1969), who solved the weakly nonlinear permanent wave equation valid for $R = O(\epsilon^{-1})$ and $W_e = O(\epsilon^{-2})$ by a perturbation technique, and by Massot, Irani & Lightfoot (1966), who solved a similar weakly nonlinear permanent wave equation with an additional criterion of least viscous dissipation. Our theory fits the measurements better than those of Lee and Massot *et al.* on wave amplitude (figure 16*a*) and propagation speed (figure 16*b*) . However the predicted wavenumber is still much higher than that observed (figure 16*c*). The partial success is encouraging, given the differences between the experimental setting and the theoretical assumptions: such as the geometric configurations, the artificially introduced perturbations; the transientness of wave overtaking and coalescence; and the magnitude of surface tension.

For nonlinear bifurcations, period-doubling has been reported by Takahama & Kato (1980), who recorded the dominant wave frequencies at fixed stations along a circular cylinder. In the recent experiments by Liu & Gollub (1993,1994) for films on a slightly inclined plane, forced perturbations were introduced at the entrance in order that regular two-dimensional waves appear. The Weber numbers are in the range of $3 < W_e < 33$. Within the first 100 cm forced waves give rise to period-1 limit cycles if the forcing frequency f is greater that f_s, but to separated solitary waves if $f < f_s$. Further downstream (120–160 cm) of the entrance, they found a different frequency threshold f_2 separating side-band instability ($f > f_2$) from subharmonic instability ($f < f_2$). When sideband instability prevails, i.e. $f > f_2$, forced waves turn chaotic further downstream; the frequency spectrum becomes broad-banded by sidebands of noise surrounding the forcing frequency. When the subharmonic instability prevails, i.e. $f < f_2$, periodic waves undergo a spatial period-doubling before complicated coalescence and splitting processes take over and lead to chaotic waves. In figure 17, we cite their results for an aqueous solution of glycerin (54% by weight) flowing down an inclined plane ($\theta = 6.4°$) with $3 < We < 30$ and $7 < R < 25$. The solid curve (f_n) denotes the forcing frequency for neutral stability determined from numerical solutions of the Orr–Sommerfeld equation and verified experimentally. For comparison the approximate threshold according to (3.6) is shown by f^-. Our theoretical threshold f^+ for period-doubling of spontaneously unstable waves originated from Hopf bifurcation is seen to be in qualitative agreement with the measured f_2. This crude agreement must be taken with caution since the forced waves in the experiments are not strictly stationary. The solitary waves predicted here resemble

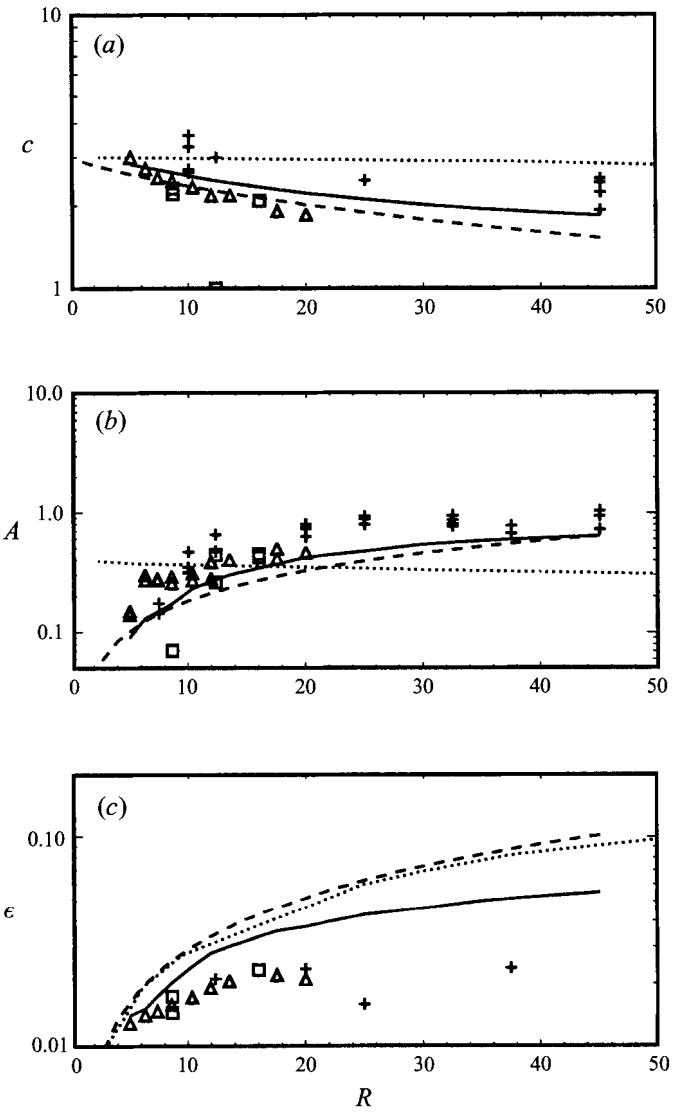

FIGURE 16. Comparison between nonlinear theories and experiments for finite-amplitude waves on the surface of vertical water film: ——, present theory; — —, theory of Lee; - - -, theory of Massot *et al.*; △, expt. by Kapitza & Kapitza; □, expt. by Jones & Whitaker; +, expt. by Stainthorp & Batt. (*a*) Phase speed c, (*b*) the dimensionless amplitude A, and (*c*) wavenumber ϵ versus R.

the observations of Liu & Gollub. However the theoretical results are found only near neutral stability for relatively low Reynolds numbers $R < 10$, while observations were made for $18 < R < 30$ with forcing frequencies much different from the natural frequency of the most unstable wave. Direct comparison cannot be made here.

For chaotic waves of large amplitude further downstream, experimental data in terms of statistical properties of vertically falling films can be found in Chu & Dukler (1974, 1975) and Yu *et al.* (1995). Although conducted on a circular cylinder of finite radius, the data by Yu *et al.* ($50 < R < 300$, $0.3 < W_e < 7$) are the closest to our theory and will be used for comparison. Shown in figure 18(*a*) are measured wave speed versus the Reynolds number. Analytical predictions of Hopf thresholds

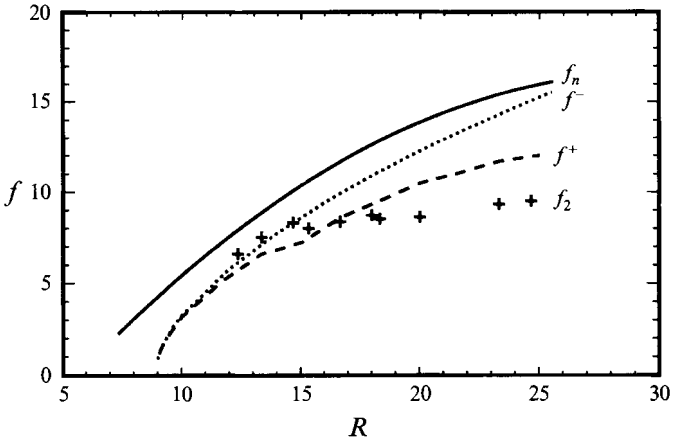

FIGURE 17. Comparison between present theory and experiments of Liu & Gollub for aqueous solutions of glycerin flowing down an incline of $\theta = 6.4°$. f_n, neutral stability frequency; f_2 (+), frequency boundary separating sideband instability and subharmonic instability; f^-, momentum integral approximation of threshhold for Hopf-bifurcation and S-W neutral stability; f^+, period-doubling bifurcation threshold.

(periodic waves) and the numerically computed limiting speed for chaotic waves from our theory are compared with the measured velocity of chaotic waves of Yu *et al.* The observed wavespeeds generally fall between these two thresholds. The theoretical results of Yu *et al.* are also included. Figure 18(*b*) compares our theory and the experiments on the RMS of the chaotic film thickness for a range of Reynolds numbers. Taking into account the difference in geometries, our theory performs no worse than the theory by Yu *et al.* based on a heuristic equation, though with a higher-order approximation of the velocity profile.

Since in most existing experiments the Reynolds number is not very high, and Weber number not very low, definitive comparisons with the present theory or its extensions should await a combination of new efforts which include new calculations by numerically solving nonlinear initial-boundary value problems for forced waves, and more experiments for naturally falling films down a long plane at large Reynolds and small Weber numbers. As an estimate for the plane length we may take a water film inclined at $\theta = (1°, 10°)$; the Reynolds numbers will be sufficiently large $R \sim (400, 200)$ if $W_e = 1$. To observe nonlinear evolutions fully the dimensionless plane length should be at least Lc_r/c_i where c_r and c_i are the real and imaginary parts of the phase velocity for the most unstable waves and can be found by solving (3.4). Estimating the wavelength to be $L = 2$ cm, $c_r = 3$ and $c_i = (0.005, 0.015)$ corresponding to the two slopes, we find the plane length to be at least $O(12, 4)$ m respectively. Also, in existing experiments the upstream discharge is maintained at the same value, hence bifurcations can only emerge from the uniform state H_I. To check experimentally the attractors bifurcating from H_{II} the upstream discharge must be suitably changed at one point during the experiment.

11. Concluding remarks

In this paper, we have studied theoretically the finite-amplitude waves of stationary form on a thin film of viscous fluid flowing down an inclined plane. Focusing on the laminar flow at rather high Reynolds numbers, and moderate Weber numbers,

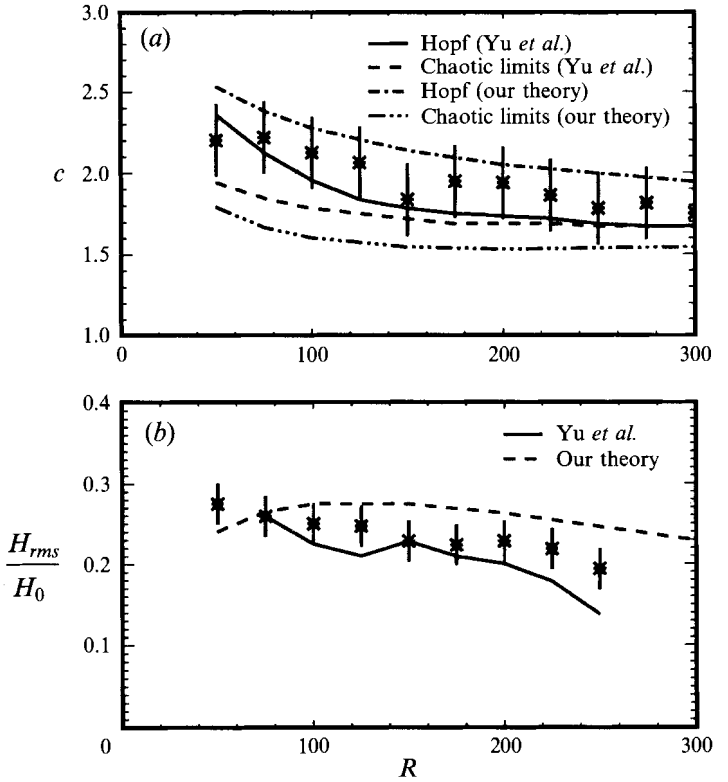

FIGURE 18. Comparison between nonlinear theories and experiments of Yu *et al.* for chaotic large-amplitude waves on flows of aqueous solutions with Kapitza number $K_a = T/(\rho g^{1/3} \nu^{4/3}) = 3550$. Experimental data are shown as *, where error bars indicate statistical uncertainty. (*a*) Propagation speed versus Reynolds number. (*b*) RMS (root-mean-square) of the time series of film thickness versus Reynolds number.

we employed approximate equations accurate to the second order in the depth-to-wavelength ratio. In the frame of reference moving with the steady wavespeed, the approximate equations reduce to a third-order dynamical system. In the regime where sinusoidal waves are linearly unstable, uniform flows, corresponding to the fixed points of the reduced system, may undergo Hopf bifurcations. Detailed local analysis and numerical integration of the dynamical system have revealed complex bifurcation scenarios after the onset of limit cycles. Different types of stationary wave profiles have been found, but their stability has not been investigated.

Comparions of the linearized part of the theory with experiments for infinitesimal waves show reasonable agreement, despite the approximation of Kármán type. For the nonlinear aspects some comparisons are made with partial success. Strict comparison requires either theoretical calculation of the transient and spatial evolution of waves forced upstream, or new experiments for naturally formed waves far downstream of a long plane. A shortcoming of the present theory is the singularity of the approximate equations. In a preliminary analysis we have found that by including terms of $O(\epsilon^4)$, terms proportional to $H_{\xi\xi\xi\xi}$ arise along with many other nonlinear terms involving lower-order derivatives. The two fixed points are still given by (4.7) and (4.8). The coefficient of $H_{\xi\xi\xi\xi}$ vanishes only when $H = 0$ which corresponds to a dry bed, or $c \leqslant 1$ in which there is no H_{II}. Thus the singularities encountered at $O(\epsilon^2)$

disappear when $O(\epsilon^4)$ terms are added†; and detailed though lengthier analysis of the fourth-order dynamical system appears worthwhile. Also since most experiments were performed on the surface of a circular cylinder of radius a comparable to the wavelength, corresponding typically to $ka < 10$, new theories accounting for the cylindrical geometry by including terms of certain order in $(ka)^{-1}$ are also desirable.

Direct numerical theories without the momentum integral approximation are of course desirable. However current numerical theories require a finite spatial domain subject to periodic boundary conditions. These practical limitations may make it difficult to study chaotic waves which are aperiodic. Finally, the stability of the stationary waves and the spanwise instability observed by Liu *et al.* (1995) deserve theoretical investigation.

This research is a byproduct of a study on mud flow supported by the US National Science Foundation Natural Hazards Mitigation Program (Grant BCS 9112748) and US Office of Naval Research Ocean Engineering Program (Grant N00014-89-J-3128). We are grateful to Dr Frédéric Dias of the University of Nice, France, for helpful comments that led to significant improvement in §8.

REFERENCES

ALEKSEENKO, S. V., NAKORYAKOV, V. YE. & POKUSAEV, B. G. 1985 Wave formation on a vertical falling liquid film. *AIChE J.* **31**, 1446–1460.

ANSHUS, B. E. & GOREN, S. L. 1966 A method of getting approximate solutions to the Orr-Sommerfeld equation for flow on a vertical wall. *AIChE J.* **12**, 1004–1008.

ATHERTON, R. W. 1972 Studies of the hydrodynamics of viscous liquid film flowing down an inclined plane. Engineer's thesis, Stanford.

BACH, P. & VILLADSEN, J. 1984 Simulation of the vertical flow of a thin, wavy film using a finite-element method. *Intl J. Heat Mass Transfer* **27**, 815–827.

BENJAMIN, T. B. 1957 Wave formation in laminar flow down an inclined plane. *J. Fluid Mech.* **2**, 554–574.

BENNEY, D. J. 1966 Long waves on liquid films. *J. Math. Phys.* **45**, 150–155.

BRAUNER, N. & MARON, D. M. 1982 Characteristics of inclined thin films. Waviness and the associated mass transfer. *Intl J. Heat Mass Transfer* **25**, 99–110.

CHANG, H.-C. 1986 Travelling waves on fluid interfaces: Normal form analysis of the Kuramoto-Sivashinsky equation. *Phys. Fluids* **29**, 3142–3147.

CHANG, H.-C. 1987 Evolution of nonlinear waves on vertically falling films – a normal form analysis. *Chem. Engng Sci.* **42**, 515–533.

CHANG, H.-C. 1989 Onset of nonlinear waves on falling films. *Phys. Fluids* A **1** , 1314–1327.

CHANG, H.-C. 1994 Wave evolution on a falling film. *Ann. Rev. Fluid Mech.* **26**, 103–136.

CHANG, H.-C., DEMEKHIN, E. A. & KOPELEVICH, D. I. 1993 Nonlinear evolution of waves on a vertically falling film. *J. Fluid Mech.* **250**, 433–480.

CHEN, L. H. & CHANG, H.-C. 1986 Nonlinear waves on liquid film surfaces–II. Bifurcation analysis of the long-wave equation. *Chem. Engng Sci.* **41**, 2477–2486.

CHU, K. J. & DUKLER, A. E. 1974 Statistical characteristics of thin, wavy films: Part II. Studies of substrate and its wave structure. *AIChE J.* **20**, 695–706.

CHU, K. J. & DUKLER, A. E. 1975 Statistical characteristics of thin, wavy films: Part III. Struture of the large waves and their resistance to gas flow. *AIChE J.* **21**, 583–593.

DEMEKHIN, E. A., TOKAREV, G. YU. & SHKADOV, V. YA. 1991 Hierarchy of bifurcations of space-periodic structures in a nonlinear model of active dissipative media. *Physica* D **52**, 338–361.

GJEVIK, B. 1970 Occurrence of finite-amplitude surface waves on falling liquid films. *Phys. Fluids* **13**, 1919–1925.

† With reference to the footnote in §4, it can be seen that the crudest $O(\epsilon^0)$ approximation for (4.1) has singularities which disappear when $O(\epsilon^2)$ terms are included.

GJEVIK, B. 1971 Spatially varying finite-amplitude wave trains on falling liquide films. *Acta Polytech. Scand. Mech. Engng* **61**, 1–16.

GUCKENHEIMER, J. & HOLMES, P. 1983 *Nonlinear Oscillations, Dynamical Systems and Bifurcations of Vector Fields*. Springer.

HYMAN, J. M. & NICOLAENKO, B. 1986 Order and complexity in the Kuramoto-Sivashinsky model of weakly turbulent interfaces. *Physica* D **23**, 265-292.

JONES, L. O. & WHITAKER, S. 1966 An experimental study of falling liquid films. *AIChE J.* **12**, 525.

JOO, S. W., DAVIS, S. H. & BANKOFF, S. G. 1991 Long-wave instabilities of heated falling films: two-dimensional theory of uniform layers. *J. Fluid Mech.* **230**, 117–146.

KAPITZA, P. L. & KAPITZA, S. P. 1949 Wave flow of thin layers of a viscous fluid. *Zh. Ekper. Teor. Fiz.* **19**, 105. Also in *Collected Papers of P. L. Kapitza* (ed. D. Ter Haar), pp. 690–709. Pergamon, 1965.

KHESHGI, H. S. & SCRIVEN, L. E. 1987 Disturbed film flow on a vertical plate. *Phys. Fluids* **30**, 990–997.

KRANTZ, W. B. & GOREN, S. L. 1971 Stability of thin liquid films flowing down a plane. *Ind. Engng Chem. Fundam.* **10**, 91–101.

LEE, J. 1969 Kapitza's method of film flow description. *Chem. Engng Sci.* **24**, 1309–1320.

LEE, J.-J. 1995 Nonlinear dynamics of a rapidlly flowing viscous fluid layer down an incline. PhD thesis, Massachusetts Institute of Technology.

LIN, S. P. 1969 Finite-amplitude stability of a parallel flow with a free surface. *J. Fluid Mech.* **36**, 113–126.

LIN, S. P. 1974 Finite-amplitude side-band instability of a viscous film. *J. Fluid Mech.* **63**, 417–429.

LIN, S. P. 1983 Film waves. In *Waves on Fluid Interfaces* (ed. R. P. Meyer), pp. 261–289. Academic Press.

LIU, J. & GOLLUB J. P. 1993 Onset of spatially chaotic waves on flowing films. *Phys. Rev. Lett.* **70**, 2289–2292.

LIU, J. & GOLLUB J. P. 1994 Solitary wave dynamics of film flows. *Phys. Fluids* **6**, 1702–1712.

LIU, J., PAUL, D. & GOLLUB J. P. 1993 Measurement of the primary instabilities of film flows. *J. Fluid Mech.* **250**, 69–101.

LIU, J., SCHNEIDER, J. B. & GOLLUB J. P. 1995 Three-dimensional instability of film flows. *Phys. Fluids* **7**, 55–67.

MASSOT, C., IRANI, F. & LIGHTFOOT, E. N. 1966 Modified description of wave motion in a falling film. *AIChE J.* **12**, 445–455.

MEI, C. C. 1966 Nonlinear gravity waves in a thin sheet of viscous fluid. *J. Math. Phys.* **45**, 266–288.

NAKAYA, C. 1975 long waves on a thin fluid layer flowing down an inclined plane. *Phys. Fluids* **18**, 1407–1420.

NAKAYA, C. 1989 Waves on a viscous fluid flim down a vertical wall. *Phys. Fluids* A **1**, 1143–1154.

NUSSELT, W. 1916 Die obserflachenkondensation des Wasserdampfes. *Z. Ver. Dtsch. Ing.* **60**, 541–552.

PIERSON, F. W. & WHITAKER, S. 1977 Some theoretical and experimental observations of the wave structure of falling films. *Ind. Engng Chem. Fundam.* **16**, 401–408.

PROKOPIOU, TH. CHENG, M. & CHANG, H.-C. 1991 Long waves on inclined films at high Reynolds number. *J. Fluid Mech.* **222**, 665–691.

PUMIR, A., MANNEVILLE, P. & POMEAU, Y. 1983 On solitary waves running down an inclined plane. *J. Fluid Mech.* **135**, 27–50.

ROSKES, G. J. 1970 Three-dimensional long waves on a liquid film. *Phys. Fluids* **13**, 1440–1445.

SALAMON, T. R., ARMSTRONG, R. C. & BROWN, R. A. 1994 Traveling waves on vertical films: Numerical analysis using the finite element method. *Phys. Fluids* **6**, 2202–2220.

SHEINTUCH, M. & DUKLER, A. E. 1989 Phase plane and bifurcation analysis of thin wavy films under shear. *AIChE J.* **35**, 177–186.

SHLANG, T. & SIVASHINSKY, G. I. 1982 Irregular flow of a liquid film down a vertical column. *J. Phys. (Paris)* **43**, 459–466.

SIL'NIKOV, L. P. 1965 A case of the existence of a denumerable set of periodic motions. *Sov. Mat. Dokl.* **6**, 163–166.

SIVASHINSKY, G. I. & MICHELSON, D. M. 1980 On irregular wavy flow of a liquid film down a vertical plane. *Prog. Theor. Phys.* **63**, 2112–2114.

STAINTHORP, F. P. & ALLEN, J. M. 1965 The development of ripples on the surface of liquid film flowing inside a vertical tube. *Trans. Inst. Chem. Engrs* **43**, 85–91.

STAINTHORP, F. P. & BATT, R. S. W. 1967 The effect of co-current and counter-current air flow on the wave properties of falling liquid films. *Trans. Inst. Chem. Engrs* **45**, 372–382.

STROBEL, W. J. & WHITAKER, S. 1969 The effect of surfactants on the flow characteristics of falling liquid films. *AIChE J.* **15**, 527–532.

TAILBY, S. R. & PORTALSKI, S. 1962 The determination of the wavelength on a vertical film of liquid flowing down a hydrodynamically smooth plate. *Trans. Inst. Chem. Engrs* **40**, 114–122.

TAKAHAMA, H. & KATO, S. 1980 Longitudinal flow characteristics of vertically falling liquid films without concurrent gas flow. *Intl J. Multiphase Flow* **6**, 203–215.

TOUGOU, H. 1981 Deformation of supercritically stable waves on a viscous liquid film down an inclined plane wall with the decrease of wave number. *Intl J. Phys. Soc. Japan* **50**, 1017–1024.

TRIFONOV, YU. YA. 1992 Two-periodical and quasi-periodical wave solutions of the Kuramoto-Sivashinsky equation and their stability and bifurcations. *Physica* D **54**, 311–330.

TRIFONOV, YU. YA. & TSVELODUB, O. YU. 1991 Nonlinear waves on the surface of a falling liquid film. Part 1. Waves of the first family and their stability. *J. Fluid Mech.* **229**, 531–554.

TSVELODUB, O. YU. & TRIFONOV, YU. YA. 1989 On steady-state traveling solutions of an evolution describing the behaviour of disturbances in an active dissipative media. *Physica* D **39**, 336–351.

TSVELODUB, O. YU. & TRIFONOV, YU. YA. 1992 Nonlinear waves on the surface of a falling liquid film. Part 2. Bifurcations of the first-family waves and other types of nonlinear waves. *J. Fluid Mech.* **244**, 149–169.

WANG, C. K., SEABORG, J. J. & LIN, S. P. 1978 Instability of multi-layered liquid films. *Phys. Fluids* **21**, 1669–1673.

WHITAKER, S. 1964 Effects of surface-active agents on the stability of falling liquid films. *Ind. Engng Chem. Fundam.* **3**, 132–145.

WIGGINS, S. 1990 *Introduction to Applied Nonlinear Dynamical Systems and Chaos.* Springer.

YIH, C.-S. 1955 Stability of parallel laminar flow with a free Surface. In *Proc. Second US National Congress of Applied Mechanics*, pp. 623–628.

YIH, C.-S. 1963 Stability of liquid flow down an inclined plane. *Phys. Fluids* **6**, 321–330.

YU, L.-Q., WASDEN, F. K., DUKLER, A. E. & BALAKOTAIAH, V. 1995 Nonlinear evolution of waves on falling films at high Reynolds number. *Phys. Fluids* **7**, 1886–1902.